Article:
Clark, ER, Porter, KE and Bryant, MG (2019) Fretting-corrosion of cardiovascular stent materials: The role of electrochemical polarisation on debris generation mechanisms. Biotribology, 18. 100093.

https://doi.org/10.1016/j.biotri.2019.100093

Fretting-corrosion of cardiovascular stent materials: the role of electrochemical polarisation on debris generation mechanisms

Emily R. Clark[1, 2], Karen E Porter[2], Michael G Bryant[1]

[1]Institute of Functional Surfaces, School of Mechanical Engineering, University of Leeds, Leeds, UK

[2]Leeds Institute for Cardiovascular and Metabolic Medicine, University of Leeds, Leeds, UK

Corresponding author

Michael G Bryant,

iFS, School of Mechanical Engineering, University of Leeds, Woodhouse Lane, Leeds, West Yorkshire, LS2 9JT

E-mail: M.G.Bryant@leeds.ac.uk

Tel: 0113 3432161

1. Introduction

Balloon angioplasty and implantation of stents has been used as a successful intervention for atherosclerosis for upwards of 40 years, yet clinical limitations persist. In-stent restenosis (ISR) accounts for about 10% of coronary stent failures, increasing to 30% in peripheral stents, one year post-implantation in the modern stent era requiring further intervention (1, 2). In-stent restenosis (ISR) is characterised by a re-narrowing of the artery post-stent implantation to such an extent that blood flow is hindered to the downstream organ (3). The principle cellular component of the arterial wall are smooth muscle cells (SMCs) which migrate towards the lumen of the artery, proliferate and secrete extracellular matrix components during development of ISR (4). The advent of drug-eluting stents (DES) has gone some way to reducing the incidence of ISR but the issue remains in a non-negligible patient subset (5). In contrast with the clinical post-failure analysis conducted in orthopaedic implants, stents with ISR are typically not removed from the patient: re-stenting or bypass grafts are used (6, 7). Post-failure inspection and analysis of the devices is therefore hampered and the true occurrence of fretting and corrosion in-vivo is unknown.

The surfaces and interfaces established during the implantation of a vascular devices are receiving increased scrutiny due to the possible adverse soft tissue effects associated with implant derived debris. Surface analysis of retrieved vascular devices has demonstrated that interfaces are susceptible to fretting-corrosion; the combined action of mechanical wear and corrosion at small displacement amplitudes. Evidence of fretting-corrosion has been observed at the braided stent strut interface (7, 8) and *in vivo* at overlapping interfaces were the use of multiple stents may be necessary to treat long lesions and those arising from complex and dynamic biomechanics, particularly in peripheral stents (6, 7, 9). Such interfaces are shown in Figure 1. Within the vasculature, stenting undergoes large deformations through haemostatic forces (e.g. pulsatile flow, pressure) and daily-living activities (e.g., leg flexion) introducing micro-displacements at overlapping or braided interfaces. Previous studies (10, 11) have shown that overlapping and braided stents (Figure 1a) exhibit evidence of wear and corrosion after laboratory simulation. This is supported by *in-vivo* observations (12, 13) (Figure 1b), in which a tentative link between metallic degradation, inflammation and ISR has been hypothesised. Therefore it

is conceivable that the nature of micro-motion and contact conditions at the interface can be incredibly transient and activity dependant.

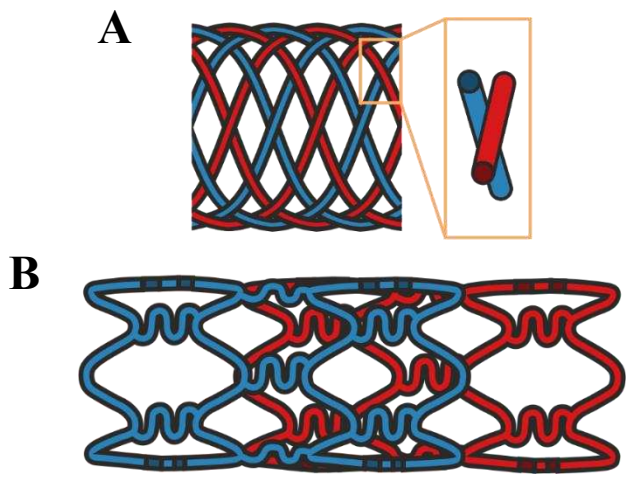

Figure 1. Schematic of fretting-corrosion interfaces in cardiovascular stents. A) Cross-wire interface in braided stents (shown with close up), more commonly used in peripheral arteries. B) Laser cut type stents in an overlapping configuration, often used for long atherosclerotic lesions or re-intervention due to ISR.

Degradation products (metal ions and nano-particles) arising from the fretting-corrosion interfaces will be released into the circulation and local tissues depending upon the degree of re-endothelialisation. Metallic debris arising from cardiovascular devices, in the form of metallic ions or bulk metal particles, has been shown to have a biological effect on cells and tissue and can mediate oxidative stress, release of proinflammatory mediators, cytotoxicity, DNA damage and functional cellular changes such as proliferation (14-17). These same biological effects are also implicated in the pathogenesis of in-stent restenosis (1, 4). To elucidate the links between device degradation and adverse biological processes, some studies have used sources such as metal chloride salts (15, 18, 19), passive corrosion through incubation under physiological conditions (20-22) or application of an electrical potential to simulate and accelerate the oxidising action of the physiological corrosive environment (16, 20). The role of tribocorrosion products (i.e. metal ions and particles) on vascular biology processes are yet to be fully considered. It is also well known that the characteristics (e.g. chemistry, thickness, stoichiometry, formation kinetics) of the passive layer on the surface of biomedical alloys, such as CoCrMo and NiTi,

67 is dependent upon the applied potential in corrosion systems (23, 24) and influences the synergistic
68 electrochemical and mechanical degradation of a metallic alloy (25-28).
69 In order to accurately assess the biological responses to metallic debris, the pathways to their production
70 must be fully considered, particular when qualifying materials and devices pre-clinically. In a
71 comprehensive review Mischler found that the potentiostatic method, whereby the system is held at a
72 nominal potential during fretting-corrosion, is the most commonly used tribo-electrochemical method
73 (29). This method has been used variously to understand the mechanisms of fretting-corrosion which
74 are representative of implanted metallic medical devices *in vivo* (23, 30-33). In reality, the potential
75 under free corrosion conditions is dynamic and evolves over time (27, 34, 35). Conducting fretting-
76 corrosion tests at the free potential of the system (or open circuit potential, OCP) has therefore more
77 recently been used to simulate the physiological fretting-corrosion mechanisms of biomaterials (36, 37).
78 The experimental methodology to understand bio-tribocorrosion mechanisms and released wear debris
79 can fundamentally alter the results. Differences in wear debris chemistry and morphology can instigate
80 differential biological effects (17, 38). Questions must be raised as to the suitability of imposing
81 electrochemical potentials to simulate corrosion in tribological contacts, its relevance to the pre-clinical
82 assessment, its implication on the nature of degradation and correlation between imposed
83 electrochemical polarisation and free corrosion conditions.
84 The aim of this study was therefore to perform a detailed tribocorrosion study investigating the effects
85 of polarisation on generated wear debris and material degradation during fretting in a simulated stented
86 physiological environment. Two primary metallic biomaterials were investigated, cobalt-chromium-
87 molybdenum (widely used biomaterial) and nickel-titanium (common vascular material) were
88 investigated in a braided stent strut model simulating the geometric considerations. The need for further
89 detailed investigation to understand the role of tribocorrosion and electrochemical potential/current
90 distributions in the vascular environment has been emphasised by leading cardiologists (39). We have
91 shown these degradation mechanisms to be detrimental to the performance of other metallic devices
92 implanted into the biological environment (40).

2. Materials and methods

Materials

Superelastic nickel-titanium, NiTi, (Nitinol, NDC, USA) and low carbon cobalt-chromium-molybdenum alloy, CoCrMo, (ASTM F1537, Heymark Metals, UK) was machined into cylindrical samples Ø6 mm to represent cylindrical braided stent struts. CoCrMo was for benchmarking due to our extensive experience with this alloy. Chemical composition of alloys used in this study are shown in Table 1 according to manufacturer. Prior to experimentation, all samples were polished to a surface roughness, R_a > 25 nm using a polishing cloth (Buehler, Germany) and graded diamond polishing pastes (Kemet International Ltd, Kent, UK), cleaned with acetone and air-dried.

Table 1. Chemical composition of low carbon CoCrMo and superelastic NiTi used in this study as stated by the manufacturer.

Element (Wt%)	Cr	Mo	Mn	Si	Ni	Fe	N	C	Co
CoCrMo	26.0 – 30.3	5.0 – 7.0	0 – 1.0	0 – 1.0	0 – 1.0	0 – 0.75	0 – 0.25	0 – 0.14	Bal
Element (Wt%)	Ni	Ti							
NiTi	55.0	45.0							

Serum-free culture media composed of Dulbecco's Modified Eagle Medium supplemented with 1% v/v L-glutamine (necessary growth factor) and 1% v/v antibiotic-antimycotic (Gibco, Renfrewshire, UK). This formulation is widely used in cell culture to simulate the physiological biochemical environment was used as the lubricant in this study (41, 42).

Fretting tribometer

Interactions between wear and corrosion were investigated using a custom-built reciprocating electromechanical fretting tribometer, previously developed, described and validated (43). A schematic for the setup is shown in Figure 2A. An electromechanical actuator provided reciprocating motion to the upper cylinder with an amplitude of 200 µm (δ_d) and was maintained at a frequency of 1 Hz, simulating that of a physiological heartbeat. δ_d = 200 µm was chosen to ensure we remain in the gross-slip regime for the duration of the test, to best represent the stent device observations (i.e. abrasion distances on the struts) (12) and FEA analysis (16). Reciprocating motion was measured by means of a fibre optic sensor fixed in the holder mounted to the base fixture of the fretting apparatus. The tangential

force (F_t) was measured throughout the experiments using a cylindrical force transducer (Kistler, USA) mounted axially to the actuator and the upper alloy cylinder. The initial normal load (F_n) at the contact between upper and lower samples was set using a force transducer (RDP Electronics, UK). A normal load of 4 N was used for each experiment (Table 2), achieving contact pressures similar to values reported by finite element analysis for overlapping cobalt-alloy stents (6). Analysis of the fretting-loop data was done according to the criteria outlined by Fouvry *et al.*(44)

Table 2. Maximum pressure at cylinder contact as calculated by Hertzian analysis.

Alloy	Young's modulus (GPa)	Poisson's ratio	Maximum contact pressure (P_{max}) (GPa)
CoCrMo	220	0.29	0.68
NiTi	34	0.33	0.21

2.3. Fretting-corrosion arrangement

A three electrode electrochemical cell was integrated into the fretting tribometer (Figure 2A). The physical connection of the upper cylinder to the lower cylinder immersed in the serum-free culture media acted as the net-working electrode (WE). A combined Ag/AgCl reference electrode (RE; +0.196V vs. standard hydrogen electrode) and Pt counter electrode (CE) (Orion, ThermoFisher Scientific, MA, US) was held in the serum-free culture media to complete the electrochemical cell. The WE, RE and CE were connected to a computer controlled potentiostat (PGSTAT101, Metrohm, Switzerland).

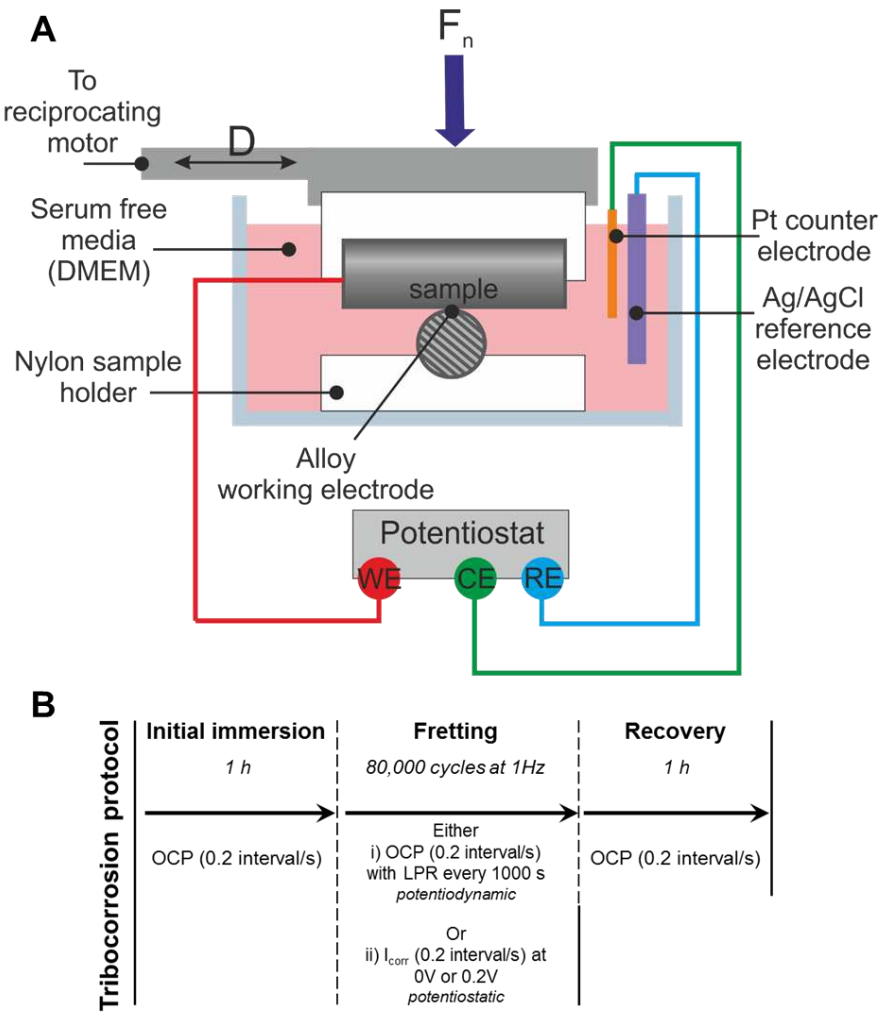

Figure 2. A) Experimental set-up of simulated braided stent strut fretting (perpendicular cylinder configuration). Hatching indicates cross section. **B)** Protocol for fretting-corrosion testing under either potentiodynamic or potentiostatic regimes.

2.3.1. Fretting-corrosion protocol

The protocol for the fretting-corrosion experiments is shown in Figure 2B. Briefly, the NiTi cylinders were polished, cleaned and dried before installation into the fretting rig in a perpendicular configuration. The serum-free culture media was then added and the upper and lower cylinders were immersed in contact with each other and left for 1 h. For each condition, the OCP was recorded in this interval. Subsequently, fretting occurred for 80,000 cycles at 1 Hz for all tests. After the fretting test, the alloy was left to recover for 1 h before the tests were dismantled and the cylinders and the serum-free culture media were collected for analysis. Serum-free culture media was frozen at -20°C to prevent dissolution of particles.

147 The fretting-corrosion behaviour of the simulated braided strut interface was evaluated under three
148 conditions:
149 Open circuit potential (OCP) with intermittent linear polarization resistance (LPR) measurements at
150 which the alloy is under free corrosion conditions enabling characterisation of the interface at
151 equilibrium. This approach has been extensively used and published in the literature for the long term
152 assessment of tribocorrosion contacts (43, 45, 46). Measurement at free corrosion potential (E_{corr}) with
153 LPR allows quantitative *in situ* dynamic corrosion measurements. LPR measurements were taken every
154 1000 s at an applied potential of ± 0 .02 V versus OCP at a scan rate of 0.25 $mV.s^{-1}$. It is widely accepted
155 that applying such a potential no permanent changes to the electrode surface are incurred (45). The scan
156 rates chosen in this study are sufficiently slow enough to eliminate any capacitive charging effects due
157 to polarisation and show no evidence of hysteresis (i.e. charging) on reversal of the potential (47). The
158 linear relationship between potential and current was used to calculate the polarisation resistance (R_p).
159 This was then used in conjunction with the experimentally determined Tafel constants and the Stern-
160 Geary (SG) relationship (Equation 1) (48) to determine corrosion current (I_{corr}) for the duration of the
161 experiment. Tafel constants for cross-cylinder contact for both CoCrMo and NiTi alloys in serum-free
162 culture media were experimentally determined under static conditions. Samples were immersed for 1 h
163 to allow the open circuit potential (OCP) to reach equilibrium before polarisation to ± 0.6 V vs RE at a
164 scan rate of 0.25 $mV.s^{-1}$ to capture the Tafel regions. For each alloy, the slope of the linear anodic and
165 cathodic regions of current in relation to overpotential (β_a and β_c respectively) were taken as the Tafel
166 constants.

$$I_{corr}=SG\left(\frac{1}{R_p}\right) \qquad (1)$$

167 Where R_p = polarisation resistance, SG = Stern-Geary coefficient, I_{corr} = corrosion current density, and

$$SG=\frac{\beta_a.\,\beta_c}{2.303\,(\beta_a+\beta_c)} \qquad (2)$$

168 Where β_a and β_c = anodic and cathodic Tafel constants respectively.
169 Potentiostatic polarization was conducted at either 0 V or 0.2 V vs RE for the duration of the experiment.
170 Tribocorrosion at increasing potentials within passive domain were selected to accelerate the anodic

processes. The current transient was recorded at 5 s intervals and both potentials were below the breakdown potential of each alloy in serum-free culture medium as experimentally determined during cyclic polarisation for determination of Tafel constants.

Optical microscopy (OM)

Optical microscopy (DM6000M, Leica, Germany) was used to inspect the wear scar and observe surface changes on both the upper and lower cylinders after fretting corrosion. As the surfaces of the cylinders were curved, a 3D montage imaging technique (Z-stack) was used to ensure all parts of the images were in focus.

Vertical scanning interferometry (VSI)

The volume loss of material from the upper and lower cylinders was determined using vertical scanning interferometry (VSI) (NPFlex, Bruker, US) with a 10x objective. Prior to VSI analysis, the cylinders were lightly cleaned using acetone to remove superficially adhered debris. The measurement area was adjusted to accommodate the varying sizes of wear scar. The volume loss was defined as the negative volume of the wear scar from the mean zero plane of the surface. The total mass loss due to both wear and corrosion mechanisms was defined as the sum of the mass loss from the upper and lower cylinders and was extrapolated from the volume loss using appropriate material density (CoCrMo: 8.4 g/cm^3 ; NiTi: 6.5 g/cm^3). VSI data was analysed using Vision 64 software (Bruker, MA, US). Cylindrical curvature and tilt was removed and a median data filter of magnitude 3 was applied.

Scanning electron microscopy (SEM)

Scanning electron microscopy with energy dispersive X-ray analysis (SEM-EDX) (Carl Zeiss EVO MA15, ZEISS, Germany) was used to determine changes in the chemical composition of the wear scar at the fretting contact. Samples were imaged with a beam intensity of 20 kV and EDX was performed at a working distance of 8 mm.

Inductively coupled plasma mass spectroscopy (ICP-MS)

Corrosion products in the media were analysed according the methods outlined by Simoes et al (49). Ion concentration and composition was measured with inductively coupled plasma mass spectroscopy

(ICP-MS). A small volume of the serum-free culture media from the fretting tests was taken and passed through a 2 kDa ultrafilter (Vivacon, Sartorius AG, Germany) at 14,000 x g for 1 h in a centrifuge to remove all particles. The ultrafiltered media was then diluted by 100x in 2% v/v nitric acid (Fluka, Honeywell, Romania) in ultrapure water and analysed for Co, Cr, Mo, Ni and Ti isotopes using ICP-MS standards for calibration for aforementioned elements (Sigma-Aldrich, USA). A matrix blank of serum-free media was also prepared to characterise background elemental signals from the media itself.

Particle analysis

A volume of 1 mL of the serum free culture media used as electrolyte during the fretting experiment was defrosted and centrifuged at 14,000 x g for 1.5 h. The supernatant was then carefully removed and the particles were resuspended in ultrapure water to remove traces of essential salts from the serum-free culture media. The centrifugation and resuspension process was repeated 5 times per sample when the supernatant was removed leaving a pellet of particles in 250 µl of ultrapure water. The particle pellets were then sonicated for 30 mins at 37°C. The particle suspension was then pipetted onto adhesive carbon SEM stubs and left to air dry. The particles were then imaged using SEM-EDX to analyse their morphology and chemical composition.

Statistical analysis

A one-way ANOVA with post-hoc Tukey test was performed for each alloy (CoCrMo and NiTi) to assess the significance of impact of the polarisation regime (OCP, 0V, 0.2V) on total mass loss and composition of ions released to the electrolyte. A p-value of less than 0.05 was considered significant for all analyses. Error bars on graphs are presented as 95% confidence intervals.

3. Results

Static cyclic polarisation

Figure 3 shows the Tafel plots obtained for CoCrMo and NiTi under static conditions. The corrosion current density (I_{corr}) and free corrosion potential (E_{corr}) determined through Tafel fitting are shown in the inset of Figure 3. Tafel constants and the associated Stern-Geary coefficient used later in the analysis of LPR data are tabulated in Table 3.

Table 3. Tafel constants of CoCrMo and NiTi alloy in serum-free culture media

Alloy	Anodic Tafel constant (β_a, V/dec)	Cathodic Tafel constant (β_c, V/dec)	Stern-Geary coefficient
CoCrMo	0.31	0.17	0.048
NiTi	0.29	0.21	0.053

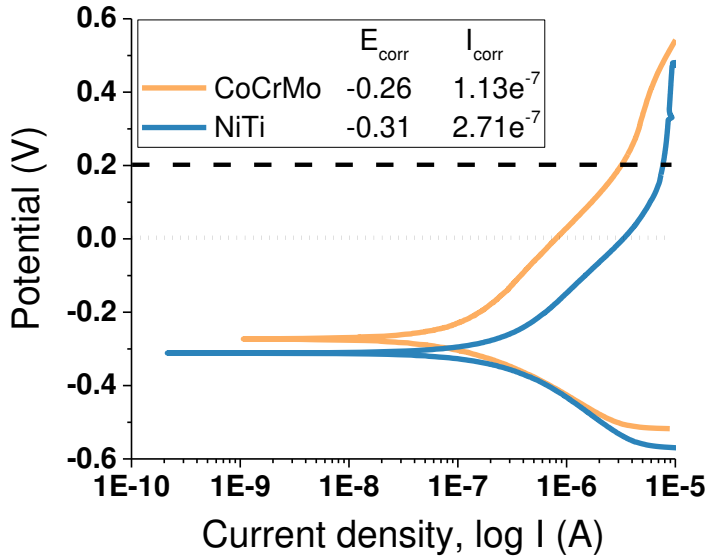

Figure 3. Polarisation curves of CoCrMo and NiTi alloy in serum-free media. Potential range -0.6 V to +0.6 V with scan rate of 0.167 $mV.s^{-1}$. Polarisation potential for potentiostatic regime shown for 0V (dotted line) and 0.2V (dashed line).

3.2. Mechanical fretting results

Representative fretting loops for CoCrMo and NiTi alloy (n=3) under polarisation regimes at OCP and held at 0V and 0.2V are shown in Figure 4. For each condition, fretting loops from intermittent cycles are shown to demonstrate the evolution of the fretting regime over time. Cumulative dissipated energy over 80,000 cycles as characterised by the mathematical area of the fretting loop is shown in Figure 5A and B for CoCrMo and NiTi respectively. Representative optical microscopy and VSI images of the wear scar for CoCrMo and NiTi under all three polarisation conditions are shown in Figure 6.

3.2.1. Fretting loops

Under all polarisation regimes, CoCrMo alloy operated within a gross-slip regime characterised by a quasi-rectangular fretting loop with a sliding / displacement ratio, $\frac{\delta_s}{\delta_d} = 0.93 - 0.95$; well within the gross-slip criteria given by Fouvry (50) . Under fretting-corrosion at OCP, CoCrMo alloy did not demonstrate any evolution in the fretting regimes over time and the loops over the course of 80,000 cycles are relatively similar with an almost indistinguishable fretting loop area (Figure 4A). When the polarisation potential was increased to 0V, fretting remained in a gross-slip regime but the fretting loop area increased over time (Figure 4B). At 0.2V polarisation potential, CoCrMo again operated in a quasi-rectangular gross-slip regime with an increase in fretting loop area over time and was overall greater than at lower polarization potentials (Figure 4C). As CoCrMo existed in a gross-slip regime for OCP, 0V and 0.2V, increasing the polarisation potential during fretting-corrosion did not therefore appear to alter the mechanism of the fretting regime. However, polarisation to both 0V and 0.2V resulted in changes to the fretting loop area over time which was not present at OCP.

The fretting conditions for superelastic NiTi alloy also exhibited a gross-slip fretting regime with $\frac{\delta_s}{\delta_d}$ varying between 0.83 and 0.95. However under such conditions the fretting loop adopts a quasi-elliptical shape with increasing tangential forces towards the end of each stroke (Figure 4D, E, F). The area of the fretting loops over the course of the fretting regime for NiTi are more consistent in comparison to those produced by CoCrMo alloy for all polarisation regimes. The trends in dissipated energy over-time were not consistent with those observed for CoCrMo and were not seen to increase with applied potential.

4. Cumulative dissipated energy

Figure 5A and B shows the cumulative energy dissipation as a function of cycles for CoCrMo and NiTi under different corrosion conditions for CoCrMo and NiTi, respectively. In general, an increase in the total energy dissipated during fretting increased with applied potential and in both material cases was non-linear with the number of cycles. When compared to CoCrMo, the energy dissipated during fretting for NiTi materials was greater.

The relationship between cumulative dissipated energy and total volume loss for CoCrMo and NiTi alloys at all polarisation potentials is shown in Figure 5C and D, respectively. For CoCrMo an increasing trend in total volume loss and total energy dissipated was observed. This relationship was not observed in NiTi alloy under all polarisation potentials (Figure 5C and D).

Wear scar morphology

Representative wear scar morphology for both alloys under all polarisation conditions is shown with both OM and VSI images in Figure 6. Independent of the wear scar size, wear scar morphology is comparable over all polarisation conditions for CoCrMo alloy (Figure 6A, B, C). CoCrMo wear scar for all conditions is characteristic of a gross slip regime in agreement with fretting loop appearance (Figure 4A, B, C). The wear scar depth, as exhibited in the VSI images, appears to increase with polarisation potential. However for NiTi alloy, wear scar morphology appears to be affected by polarisation potential. At OCP, the wear scar directionality is relatively clear – parallel to the cylinder length for the top sample and perpendicular for the base (Figure 6D). As polarisation potential is increased, the wear scar surface became more heterogeneous and the directionality became indistinguishable at 0.2V (Figure 6E, F). CoCrMo alloy typically exhibited a classically abrasive wear scar morphology whilst NiTi showed an increasingly adhesive scar morphology with increasing potential. In summary, the inherent wear scar morphology was overtly altered in NiTi fretting by polarisation, but not for CoCrMo alloy.

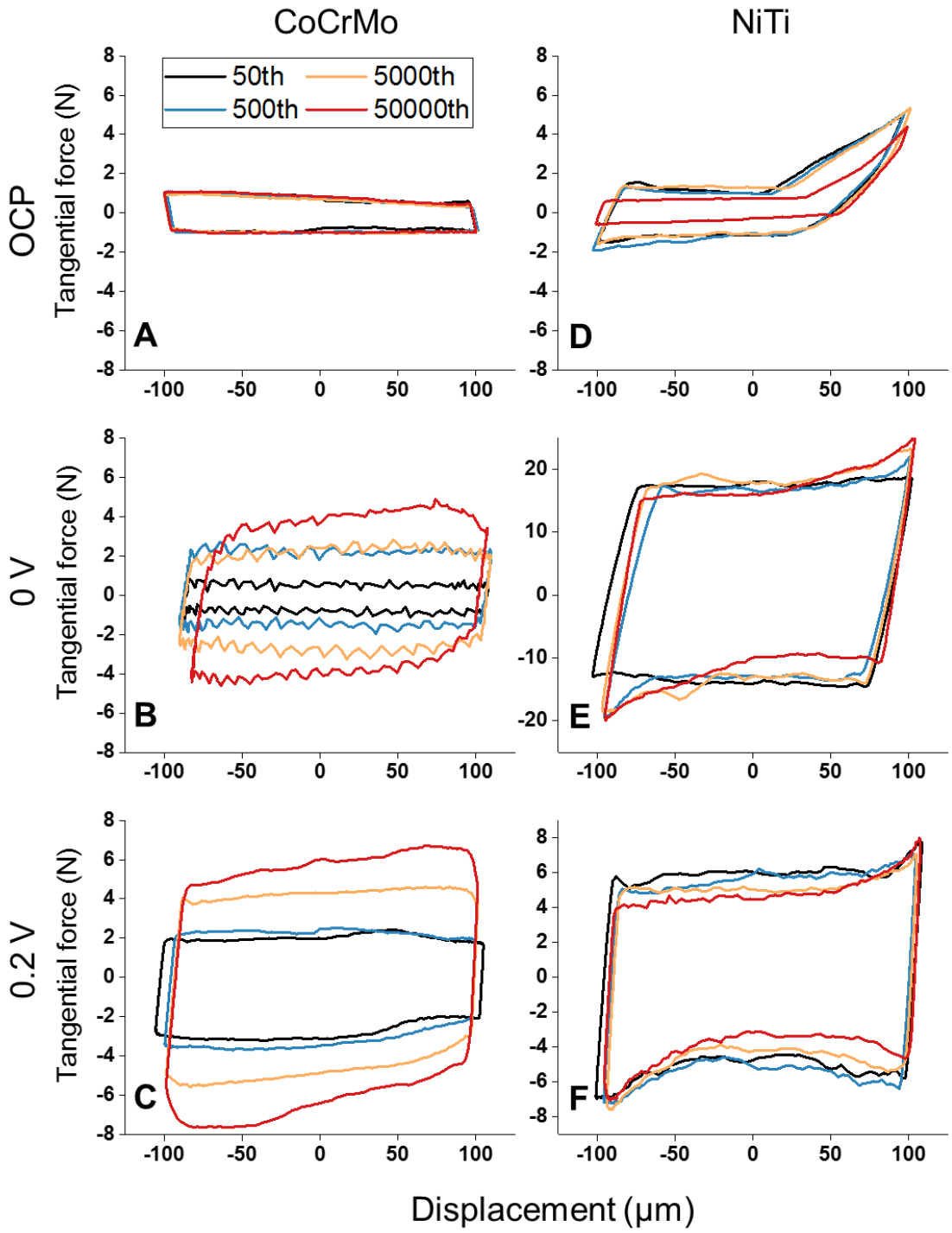

283

284 **Figure 4.** Representative fretting loops from the 50th and 50,000th cycle for CoCrMo and NiTi alloy
285 in polarisation regimes at OCP and held at 0V and 0.2V.

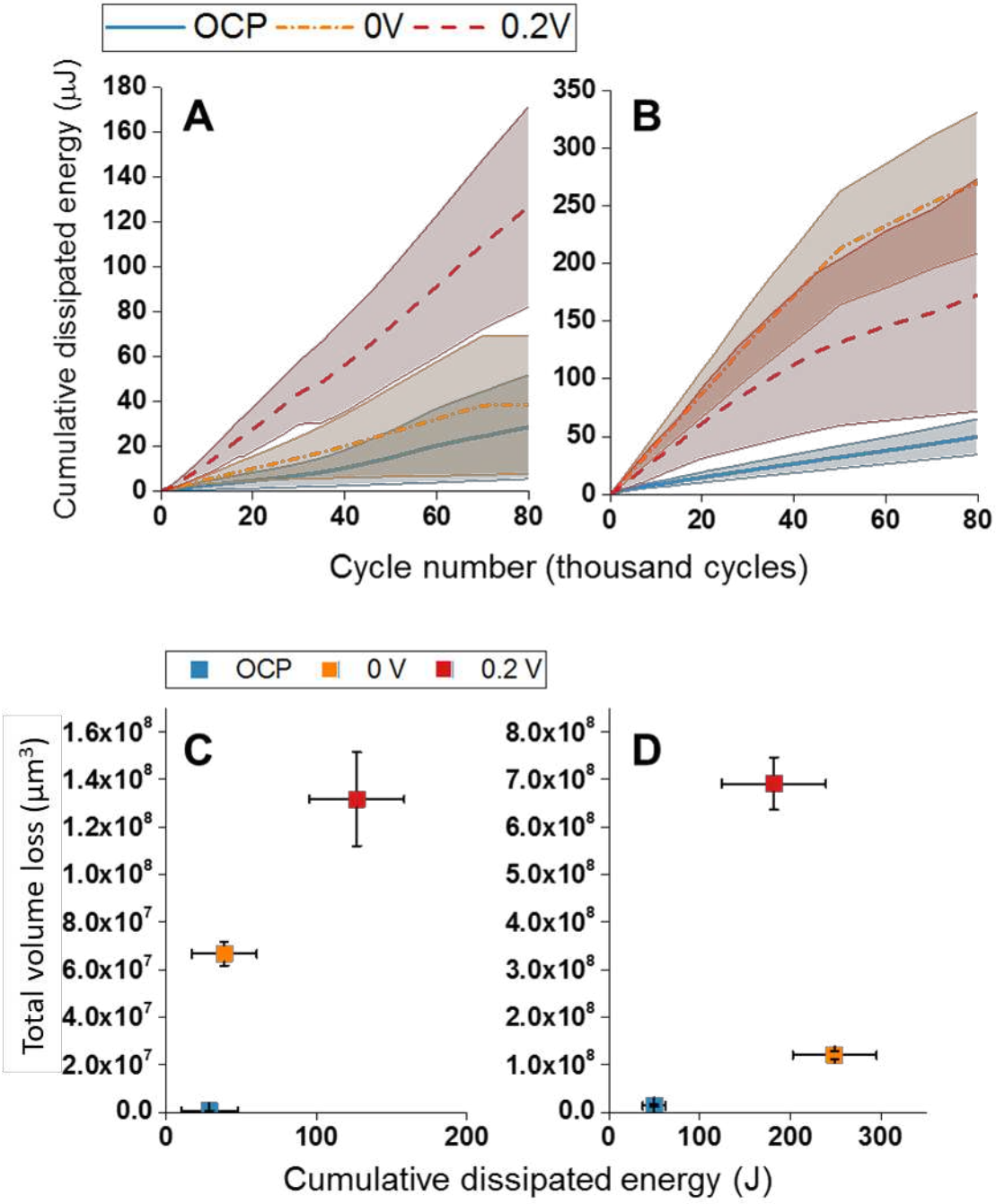

286

287 **Figure 5.** Cumulative dissipated friction energy over time for A) CoCrMo and B) NiTi alloy for fretting-
288 corrosion under OCP and held at 0V and 0.2V (n=3). Cumulative dissipated energy also shown as a
289 function of total wear volume for C) CoCrMo (red line = linear fit, adj. $R^2 = 0.92$) and D) NiTi (red line
290 = exponential fit) alloy. Data shown is mean ± 95% confidence intervals (Panels A and B: shaded area).

291

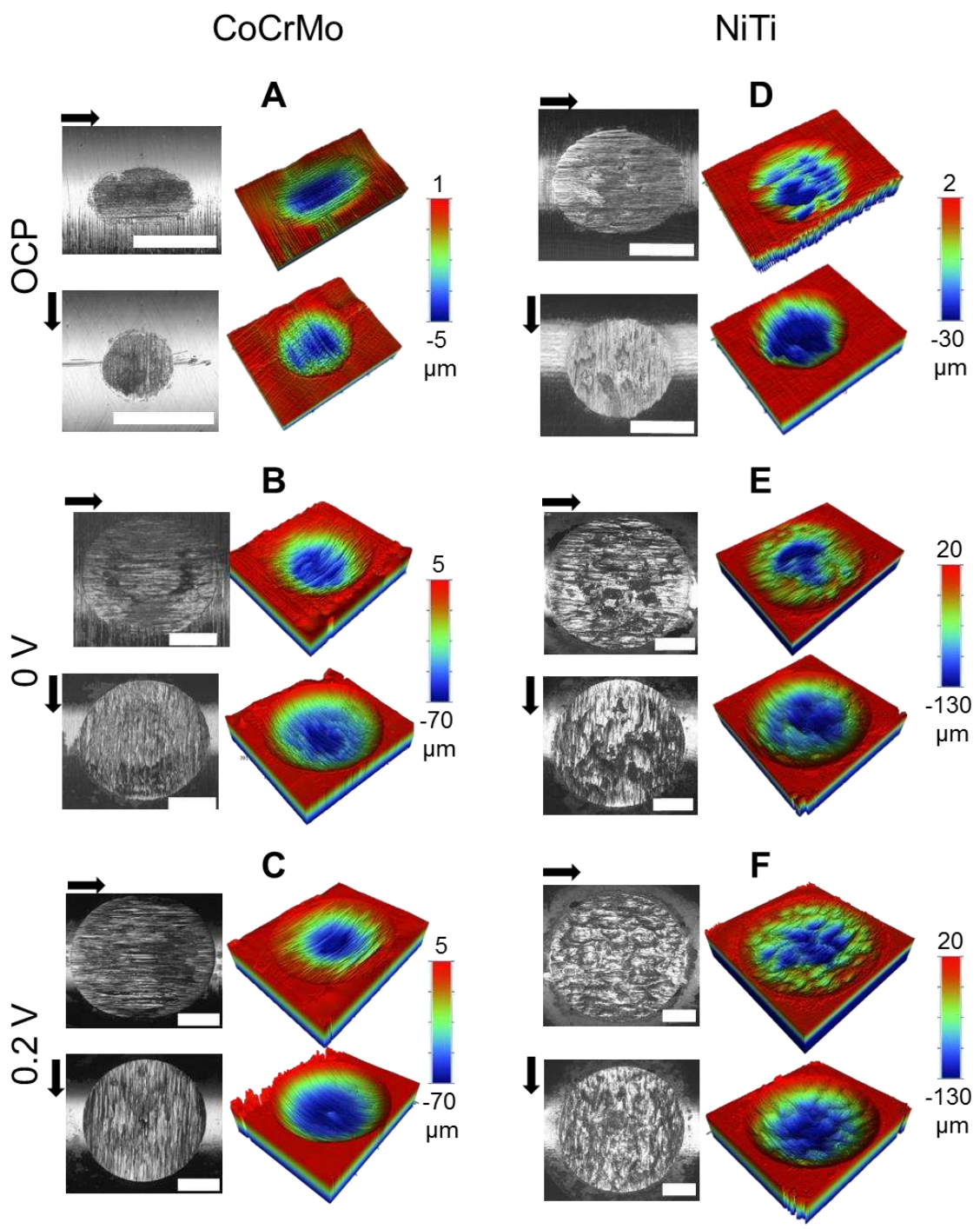

Figure 6. Wear volume loss and wear scar morphology as shown by VSI and microscopy respectively for CoCrMo and NiTi in all polarisation conditions. A) CoCrMo at OCP. B) CoCrMo at 0V potentiostatic. C) CoCrMo at 0.2V potentiostatic. D) NiTi at OCP. E) NiTi at 0V potentiostatic. F) NiTi at 0.2V potentiostatic. Scale bar for microscopy images = 500µm. Top and bottom images for each panel represent top and bottom samples respectively. Sliding direction is horizontal for the top samples and vertical for the bottom samples (arrows).

Corrosion results

4.2.1. Evolution of OCP

Representative OCP readings for both CoCrMo and NiTi alloy are shown in Figure 7A. The OCP prior to initiation of sliding was more noble for CoCrMo when compared to NiTi. For both alloys, there is a 4.2. sharp decrease in OCP upon initiation of sliding indicative of abrasion of the passive layer. There is a persistent decrease in OCP for CoCrMo and NiTi over time. Recovery of the OCP was observed when fretting was ceased although did not recover to values observed before the application of fretting suggesting changes in oxide chemistry and increased susceptibility to corrosion. (23, 29, 43, 51).

4.2.2. Potentiostatic tests

Representative current transients obtained under potentiostatic conditions (those held at 0V and 0.2V) are shown in Figure 7B. There was a consistent increase in current for both CoCrMo and NiTi at both 0V and 0.2V upon initiation of sliding, indicating abrasion of the passive layer. For both alloys an increase in polarisation potential from 0V to 0.2V typically resulted in a consistently higher current although this increase was much starker in NiTi. Generally NiTi reached higher sustained currents than CoCrMo (Figure 7B). The cumulative charge for all experiments is given in Figure 7C. For CoCrMo, increasing the polarisation potential from 0V to 0.2V typically did not result in significant increase in cumulative charge. However, both polarised conditions have greater cumulative charge compared to experiments conducted at OCP. NiTi alloy was more sensitive to an increase in polarisation potential, resulting in a significant increase in both cases – particularly stark when increased to 0.2V.

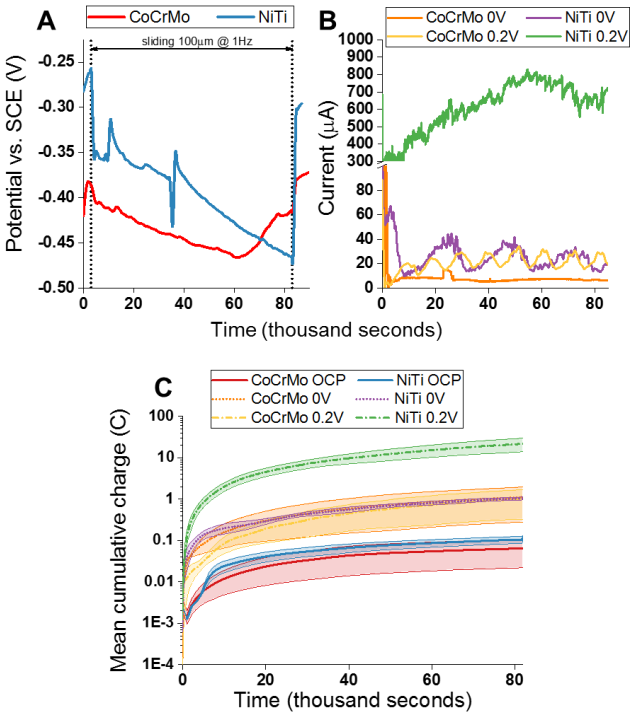

322

323 **Figure 7. A)** Representative open circuit potential (OCP) readings for CoCrMo and NiTi cross cylinder
324 fretting corrosion. Samples were left to reach free potential for 1 h prior to initiation of sliding for
325 80,000 cycles at 1 Hz. Subsequently, samples were left for 1 h to recover. Linear polarization
326 measurements (OCP ± 0.02 mV) were conducted every 1000 s for the duration of the experiment. **B)**
327 Representative current transients for potentiostatic experiments held at 0V and 0.2V. **C)** Cumulative
328 charge for all experiments using Stern-Geary relationship with intermittent LPRs to give I_{corr} for OCP
329 experiments. Data shown is mean ± SEM (shaded area).

330

4.3.

331 **Material loss**

332 Total material loss (M_{total}) was quantified using VSI and nominal alloy densities. The contributing
333 mechanisms to mass loss are presented later in this paper in Figure 13. There was no significant
334 difference in total mass loss between the potentiostatic regimes for CoCrMo alloy (0.73 ± 0.42 mg at
335 0V; 1.21 ± 0.49 mg at 0.2V). Samples from both potentiostatic regimes had significantly greater total
336 mass loss vs. those which underwent fretting-corrosion at free corrosion potential (4.70 ± 0.74 µg,
337 $p<0.05$ vs. 0V and $p<0.001$ vs. 0.2V). NiTi alloy appeared to be particularly susceptible to an increase
338 in polarisation potential: total mass loss at 0.2 V (6.68 ± 1.85 mg) was significantly greater than that at
339 0V (0.79 ± 0.06 mg, $p<0.001$) and OCP (0.09 ± 0.03 mg, $p<0.001$). However, total mass loss at OCP
340 and 0V was not significantly changed. Total mass loss for both CoCrMo alloy and NiTi alloy were

relatively similar under both OCP and 0V regimes. However, at 0.2V NiTi had a mean 5.5-fold increase in total mass loss compared to CoCrMo alloy.

Wear scar chemistry

Wear scar chemical composition and topography was analysed with SEM-EDX. Representative SEM images of the wear scar and SEM-EDX maps of the wear scar chemistry for each polarisation condition for CoCrMo are shown in Figure 8 and those for NiTi are shown in Figure 9. Elements such as phosphorus, potassium, calcium and chlorine were seen in the contact areas after fretting-corrosion. For CoCrMo alloy, increasing the polarisation potential from OCP up to 0.2V resulted in a stronger correlation of chromium with oxygen (Figure 8C, F, I). Molybdenum signal remained generalised over the whole wear scar under all polarisation conditions. At 0V only there was localised formation of phosphorous which was more generalised at both OCP and 0.2V. Under OCP conditions, a build-up formed at the edge of the wear scar which is noticeably absent under both 0V and 0.2V conditions. Interestingly, the element signals present differ between polarisation potential: calcium is only detected at OCP and potassium is solely detected at 0V.

For NiTi alloy, in all polarisation conditions, the formation of complexes within the fretting contact were dominated by titanium (Figure 9; Panel C, F and I). Formation of titanium oxide film occurred generally over the wear scar, whereas sulphur and carbon complexes formed in specific locations at OCP and 0.2V respectively. Increasing the polarisation potential from instigates inherent changes in wear scar chemistry. At OCP, oxygen correlates with sodium, phosphorous, calcium, potassium and chlorine. However at 0V and 0.2V, carbon is detected which is not present at OCP. Conversely sodium, sulphur and calcium are only detected at OCP and are not present at 0V and 0.2V (Figure 9C, F, I). Contrary to CoCrMo, for NiTi a build-up of predominantly elements only contained within the serum-free media (O, C, P, K) rather than those contained within the bulk metal (Ni, Ti) can be observed at anodic polarisation conditions around the edge of the contact whereas this was absent at OCP (Figure 9; Panels A, D and G).

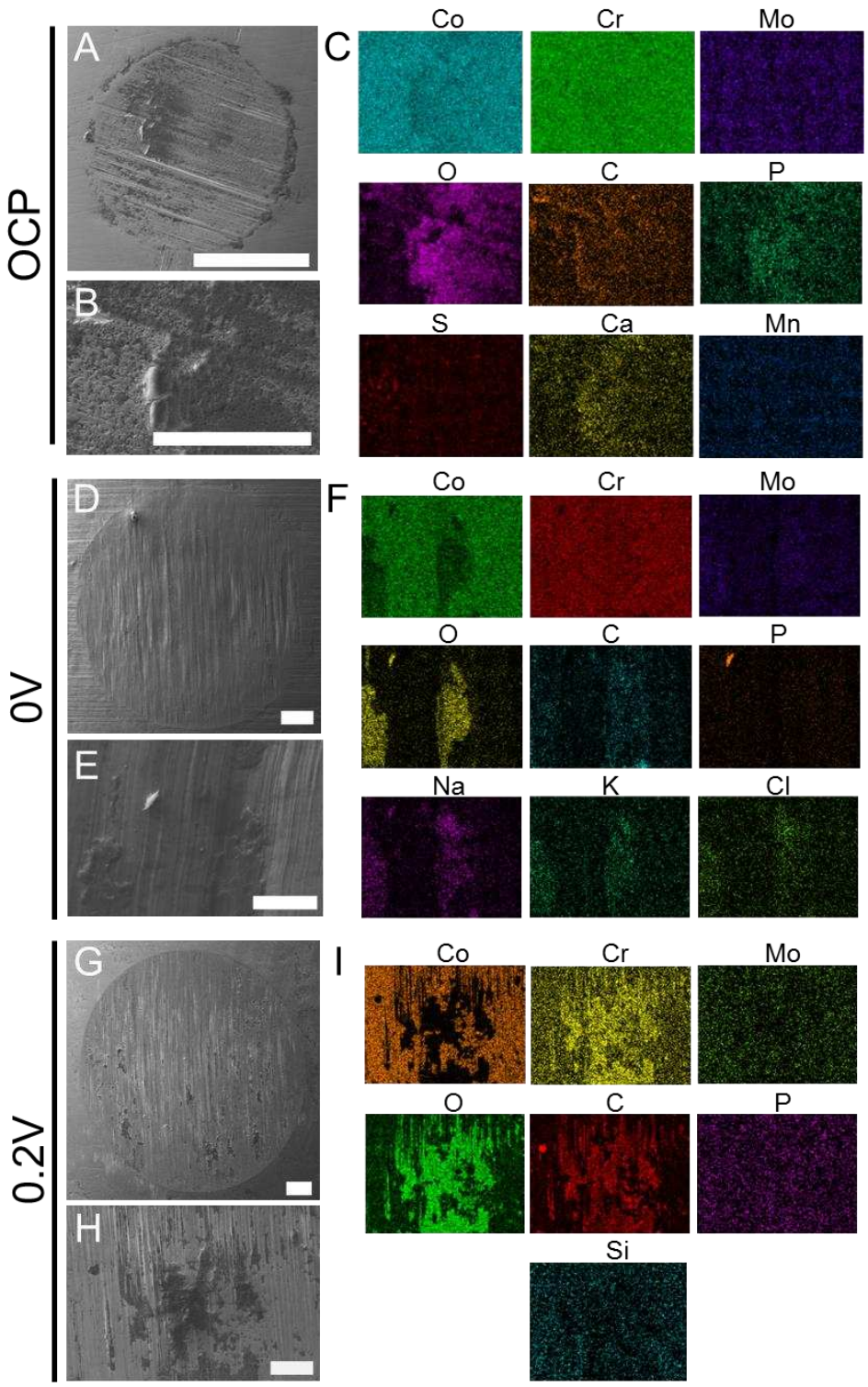

366

367 **Figure 8.** Representative SEM images and SEM-EDX maps for CoCrMo alloy for all polarisation
368 conditions. A) SEM image of complete wear scar at OCP. B) SEM image of wear scar detail at OCP.
369 C) SEM-EDX map for wear scar chemistry at OCP. D) SEM complete wear scar 0V. E) SEM detail
370 wear scar 0V. F) SEM-EDX map 0V. G) SEM complete wear scar 0.2V. H) SEM detail wear scar 0.2V.
371 I) SEM-EDX map 0.2V. Panels A, D, G: scale bar = 200µm. Panels B, E, H: scale bar = 100µm.

372

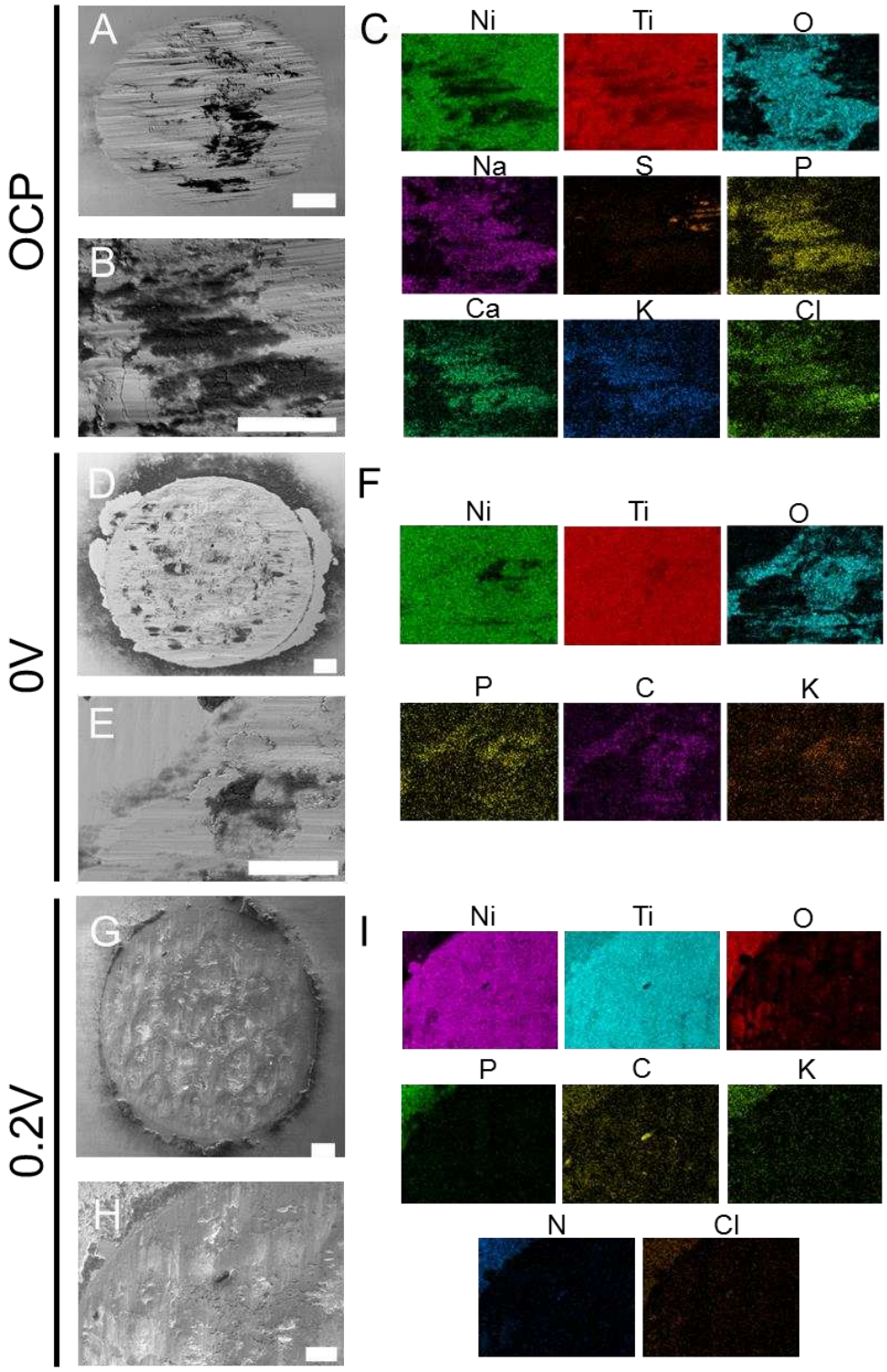

373

374 **Figure 9.** Representative SEM images and SEM-EDX maps for NiTi alloy for all polarisation
375 conditions. A) SEM image of complete wear scar at OCP. B) SEM image of wear scar detail at OCP.
376 C) SEM-EDX map for wear scar chemistry at OCP. D) SEM complete wear scar 0V. E) SEM detail
377 wear scar 0V. F) SEM-EDX map 0V. G) SEM complete wear scar 0.2V. H) SEM detail wear scar 0.2V.
378 I) SEM-EDX map 0.2V. Panels A, D, G: scale bar = 200µm. Panels B, E, H: scale bar = 100µm.

379

Ion release into media

Ion release to the electrolyte was determined through ICP-MS for CoCrMo and NiTi alloys at each polarisation condition (OCP, 0V and 0.2V) after centrifugation. The composition of ion release is shown in Figure 10. For CoCrMo, the total levels of ions released to the media was not significantly different across all polarisation regimes (11.1 ± 4.7 ppm, 2.9 ± 1.3 ppm and 10.5 ± 2.8 ppm for OCP, 0V and 0.2V respectively). However the composition of the ion release was affected. Ion release for fretting-corrosion of CoCrMo was dominated by cobalt in both potentiostatic polarisation conditions; 80% at 0V and 92% at 0.2V. Ion dissolution to media was dominated by chromium for CoCrMo alloy at OCP, at a level of 89% with Co dissolution dropping significantly to 2% ($p<0.001$).

Total ion release for NiTi alloy was also not found to be different at OCP (0.22 ± 0.05 ppm) compared to 0V (1.9 ± 0.4 ppm). However, the total ion release at 0.2V (160 ± 79.6 ppm) was much higher and was significantly increased compared to both that at OCP and 0V ($p<0.01$). Ion release for NiTi alloy was approximately stoichiometric at OCP (57% Ni), but under electrochemical polarisation was dominated by Ni, increasing with polarisation potential; 71% at 0V and 99% at 0.2V. The proportion of Ni ions which were released into the media was significantly increased at both 0V ($p<0.05$) and 0.2V ($p<0.001$) versus OCP.

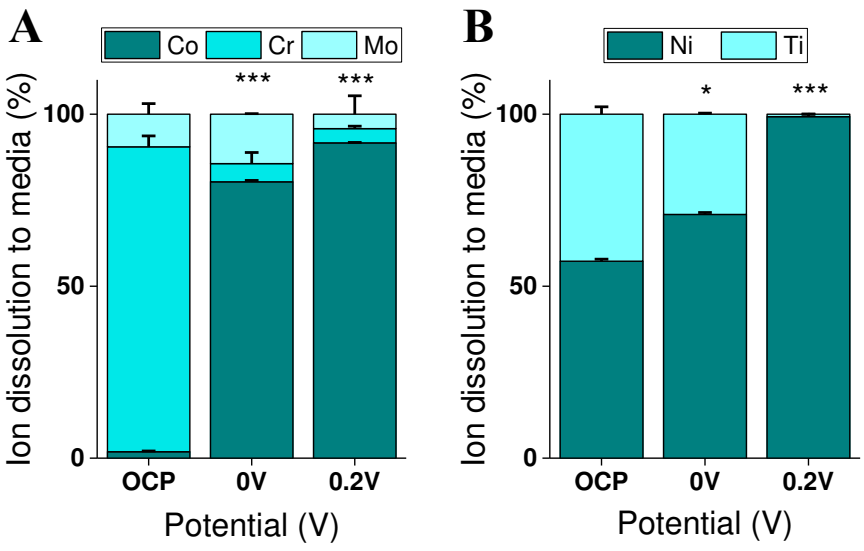

Figure 10. Proportion of ion release as measured through ICP-MS for A) CoCrMo alloy and B) NiTi alloy. *p<0.05, ***p<0.001, one-way ANOVA with post-hoc Tukey test for A) Co ions and B) Ni ions. Data shown is mean ± 95% confidence intervals.

4.6. Particle morphology and composition

Particle morphology and composition was determined with SEM-EDX imaging. For CoCrMo alloy, increasing polarisation potential had a clear impact on particle morphology. At OCP, for all three tests which were performed, particles tended to be in the micron to sub-micron range and were typically smooth and relatively heterogeneous (Figure 11A). However, when analysed with SEM-EDX, it was not possible to identify any of the bulk metal elements (Co, Cr and Mo) in the particles after removal of soluble salts by washing with ultrapure water (Figure 11B). Instead, particles showed signals for oxygen, phosphorous and calcium which are all elements present in the serum-free culture medium electrolyte.

For the potentiostatic conditions, at 0V particles were typically in the micron to sub-micron range, although some larger 'clusters' were identified (Figure 11C). Chromium, oxygen and phosphorous rich particles were observed, with no evidence of cobalt being observed. Silicon was also detected which was not present in the wear scar interface of the bulk alloys (Figure 11D). At 0.2V, the particle morphology appeared to be less 'particulate' and was generally seen to have clusters of larger particles which were more irregular in shape (Figure 11E). The chemistry of the particles was relatively equivalent to that at 0V, with good correlation of chromium, oxygen and phosphorous and an absence of cobalt (Figure 11F).

For NiTi alloy, at OCP particles were typically smooth, uniform and in the single micron to nanoparticle range although this was occasionally interspersed with large multi-micron scale particles (Figure 12A). The smallest particles were comprised of bulk NiTi, demonstrating EDX signals for both nickel and titanium (Figure 12B). Larger particles showed oxide signals. At 0V, particle morphology was generally flakier; particles were rougher and flatter than in in OCP condition (Figure 12C). Particles ranged in nanometres to multi-micron in size. Composition at 0V polarisation was similar to that at OCP, where particles typically demonstrated nickel, titanium and oxygen signals (Figure 12D). Fretting tests at 0.2V polarisation were markedly different from the other conditions in that they tended to be larger and had a heterogeneous more 'powdery' appearance (Figure 12E). Nickel signals from EDX tended to be weaker than those from particles at other polarisation conditions and also showed complexing with calcium and phosphorus in addition to oxygen (Figure 12F).

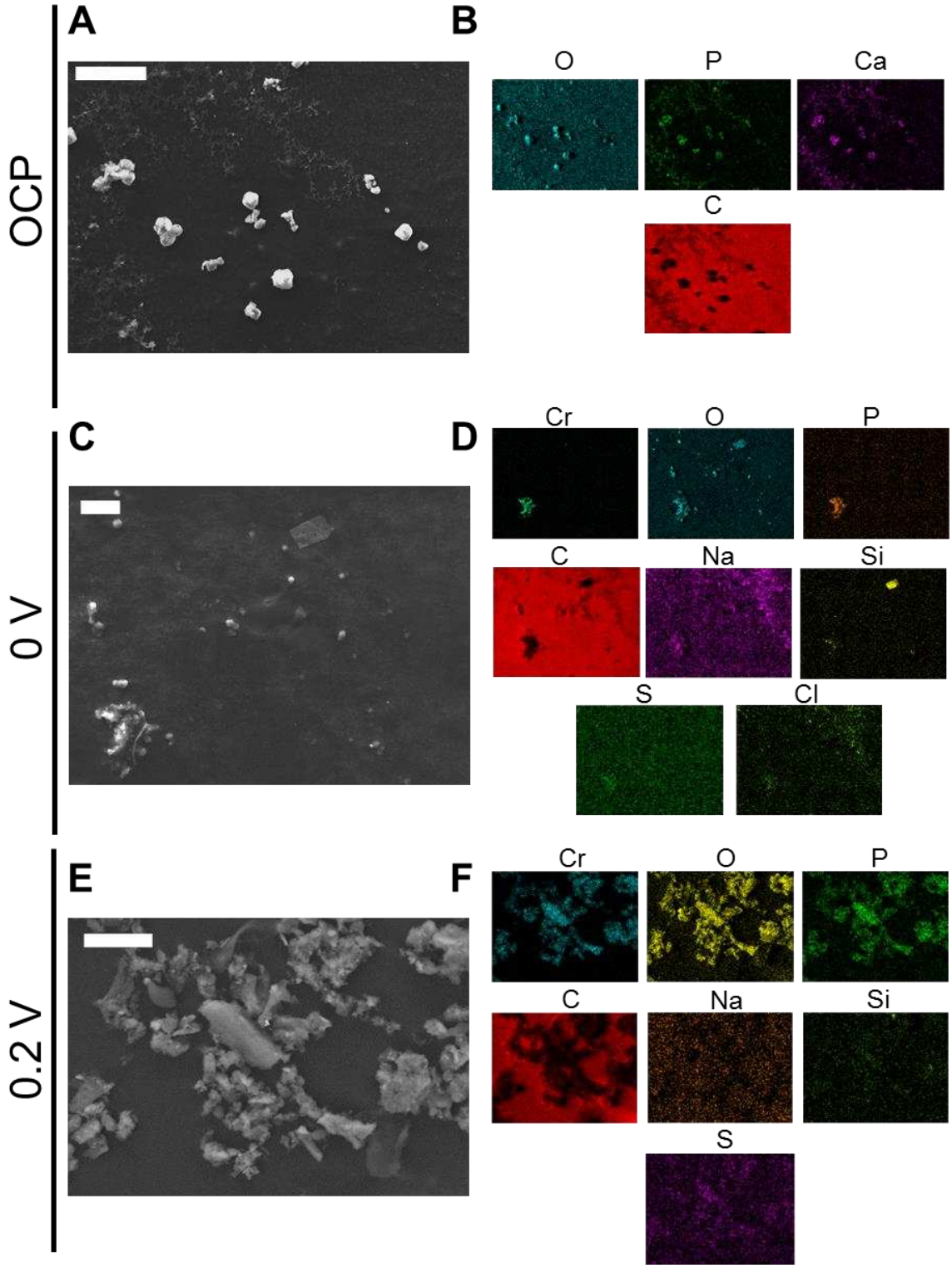

429

430 Figure 11. Representative SEM images and SEM-EDX maps for wear particles from CoCrMo alloy
431 fretting experiments. A) SEM image of wear particles from CoCrMo fretting at OCP. B) SEM-EDX
432 map for particle chemical composition at OCP. C) SEM wear particles CoCrMo 0V. D) SEM- EDX
433 map wear particles CoCrMo 0V. E) SEM wear particles CoCrMo 0.2V. F) SEM-EDX map wear
434 particles CoCrMo 0.2V. Scale bar for all images = 25µm.

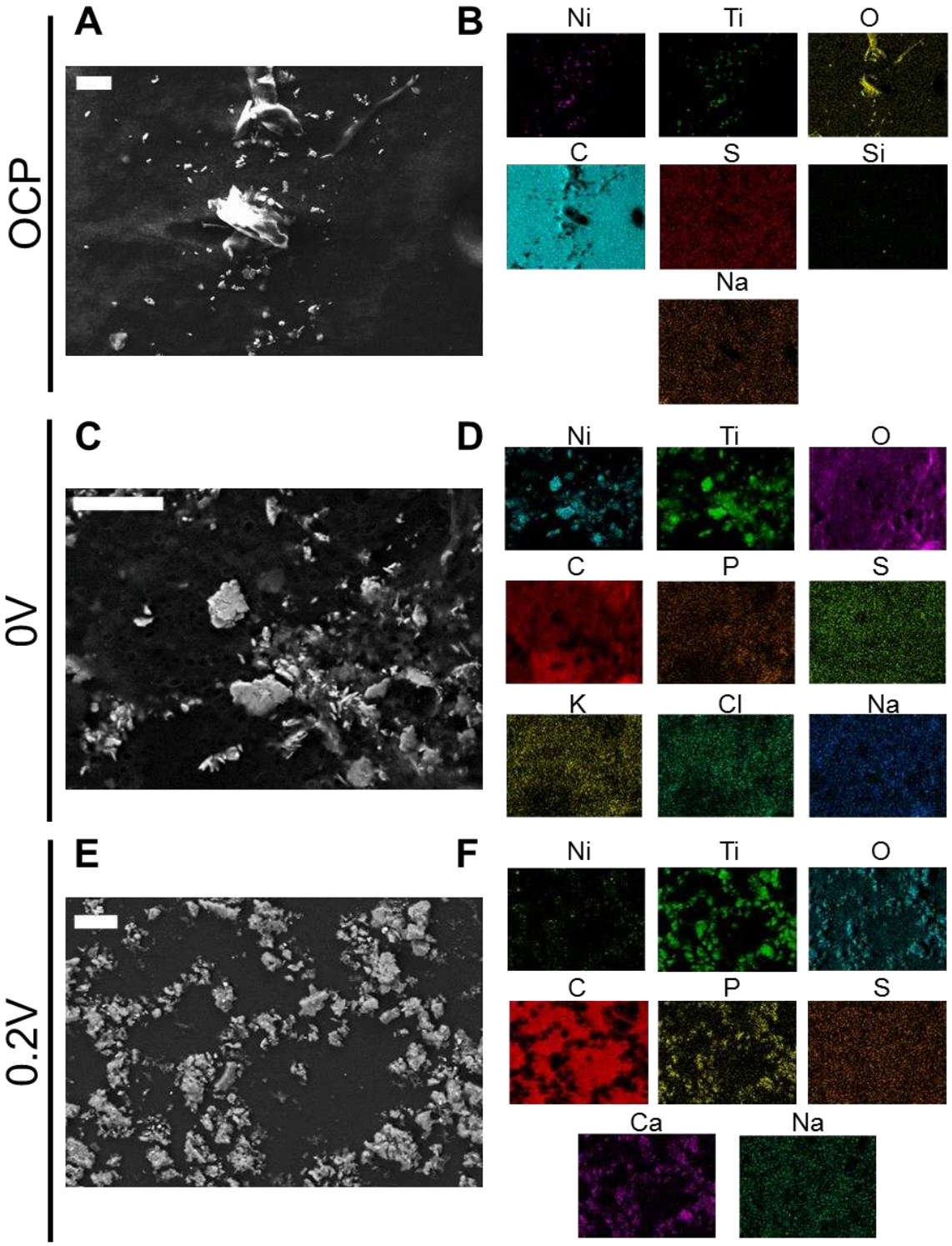

435

436 Figure 12. Representative SEM images and SEM-EDX maps for wear particles from NiTi alloy fretting
437 experiments. A) SEM image of wear particles from NiTi fretting at OCP. B) SEM-EDX map for particle
438 chemical composition at OCP. C) SEM wear particles NiTi 0V. D) SEM-EDX map wear particles NiTi
439 0V. E) SEM wear particles NiTi 0.2V. F) SEM-EDX map wear particles NiTi 0.2V. Scale bar for all
440 images = 25µm.

441

442

5. Discussion

This study has investigated the role of fretting -corrosion on the degradation of materials commonly used in biomedical applications. The resultant ionic and particulate debris has been quantified as a function of applied over-potential. Fretting-corrosion at the stent-strut interface has been observed clinically, with the roles of metal ion and particle release hypothesised to contribute to ISR processes (16). Whilst the role of metal ion release into the cardiovascular environment and prevalence in clinical complications is not fully understood, it is accepted that toxic and sub-toxic release of metal derived debris may induces some adverse clinical effects. Furthermore, pre-clinical assessment studies typically treat wear and corrosion in isolation (10, 14), only revealing part of the story concerning the degradation of metallic surfaces. Key findings from this study can be summarised as follows:

i) The synergistic interaction of wear and corrosion are inevitable at contacting metal-metal interfaces when subjected to micro-motion in a conductive biological environments. The presence of fretting increasing the rates of corrosion. This leads to the production of metallic ions and particulates; the nature of which are dependent on the tribological and corrosive conditions applied.

ii) The electrochemical parameters used to facilitate measurements of current transients associated with fretting-corrosion can significantly affect the mechanisms of degradation and the nature of the debris generated. This raises question around the suitability of imposing electrochemical potentials in the preclinical assessment of materials and how we interpret such data.

5.1. The role of applied potential on degradation mechanisms

The degradation mechanism in fretting-corrosion arises from a synergistic interaction between mechanical wear (M_{mech}) and corrosion due to intermittent depassivation (M_{chem})(29). Considering this, the relative contributions to total material loss in fretting-corrosion can be estimated using the Equations 3 – 5. M_{mech} is subdivided into M_{wear}, a purely mechanical component, and M_{cw} representing the synergy between corrosion and wear (corrosion-enhanced wear). Equally M_{chem} is subdivided into M_{corr}, a purely chemical component, and M_{wc} representing the synergy between wear and corrosion (wear-enhanced

corrosion)(45). This approach is widely use in the area on tribocorrosion to estimate material mass loss contributions. Bryant and Neville (45) have recently provided a detailed analysis of the approaches in calculating material loss mechanisms in fretting-corrosion contacts and the limitations of this approach (45, 52). Corrosion currents (Figure 7) were converted into corrosion mass losses where 'm' is the mass liberated at the anode, 'Q' is the charge passing through the WE, 'M' is the molar mass of the element, 'z' is the dissolution valence and 'F' is Faraday's constant equal to 96,480 C mol^{-1}. For each alloy, it was assumed that there was stoichiometric dissolution of the component elements, giving molar mass (M) as 58.0 $g.mol^{-1}$ for CoCrMo and 53.8 $g.mol^{-1}$ for NiTi. Equally, the dissolution valence (z) was assumed to be 2.0 for CoCrMo and 2.9 for NiTi. Applying Faraday's law to the electrochemical data recorded throughout the duration of the fretting-corrosion experiments allowed conversion to mass loss equal to chemical wear (M_{chem}). The total mass loss (M_{total}) was determined using VSI and known alloy density and their difference represented mass loss due to mechanical wear (M_{mech}).

$$M_{total} = M_{mech} + M_{chem} \quad (3)$$

$$M_{mech} = M_{wear} + M_{cw} \quad (4)$$

$$M_{chem} = M_{corr} + M_{wc} \quad (5)$$

$$m = \frac{Q \times M}{z \times F} \quad (6)$$

Figure 13 shows the total mass loss (M_{total}) and their contributors using the approach described above (Equation 6) for CoCrMo and NiTi alloys. At OCP, 0V and 0.2V, CoCrMo material loss mechanisms were dominated by corrosion related processes. However with increasing applied polarisation potential the role of mechanical contributors in the fretting-corrosion system increased (Figure 13A). As mentioned above, M_{mech} still contains a corrosive contributor. Corrosion enhanced wear processes, whereby mechanical material losses are enhanced through corrosion processes (e.g. by increased surface roughness), may contribute to this increase. With increased applied potential, higher currents were observed which will in turn influence the nature of topography within the contact as evidenced in Figure 6.

492 Conversely, NiTi operated in a regime where M_{mech} was dominant, with corrosive contributions
493 increases with applied potential due to the increased over-potential driving the magnitude of current
494 evolved during abrasion. An increase in polarisiation potential appears to increase the susceptibility of
495 NiTi to corrosive-dominated wear as demonstrated by the increase in corrosion current coupled with no
496 change in dissipated frictional energy. Nevertheless, the wear degradation pathway tended towards a
497 more wear-dominant regime with increasing polarisation potential as exhibited by the relative
498 contributions to wear (Figure 13). However, the fretting-corrosion system exists as a synergy of wear
499 and corrosion: although the corrosion currents exponentially increased with polarisation potential,
500 mechanical depassivation is still required for this wear-enhanced corrosion. Lukina *et al.* demonstrated
501 that under fretting corrosion, NiTi is particularly susceptible to very high corrosion currents compared
502 to other alloys such as biomedical titanium and CoCrMo (53). Kosec *et al.* also concluded NiTi was
503 susceptible to increased material degradation under wear-corrosion synergy conditions as opposed to
504 static corrosion due to cyclic depassivation of the oxide film (54). In the case of overlapping NiTi stents,
505 Trépanier *et al.* showed that the effect of wear on corrosion was comparable between stainless steel and
506 NiTi (55). However, in this case, the wear-corrosion synergy was not considered and specimens
507 underwent fretting wear damage and then were subsequently subjected to cyclic polarisation testing.
508 NiTi is comparable to stainless steel in its ability to repassivate wear damage to the stent surface, but
509 the present study shows that NiTi is more susceptible than CoCrMo to the wear-corrosion synergy under
510 polarisation.
511

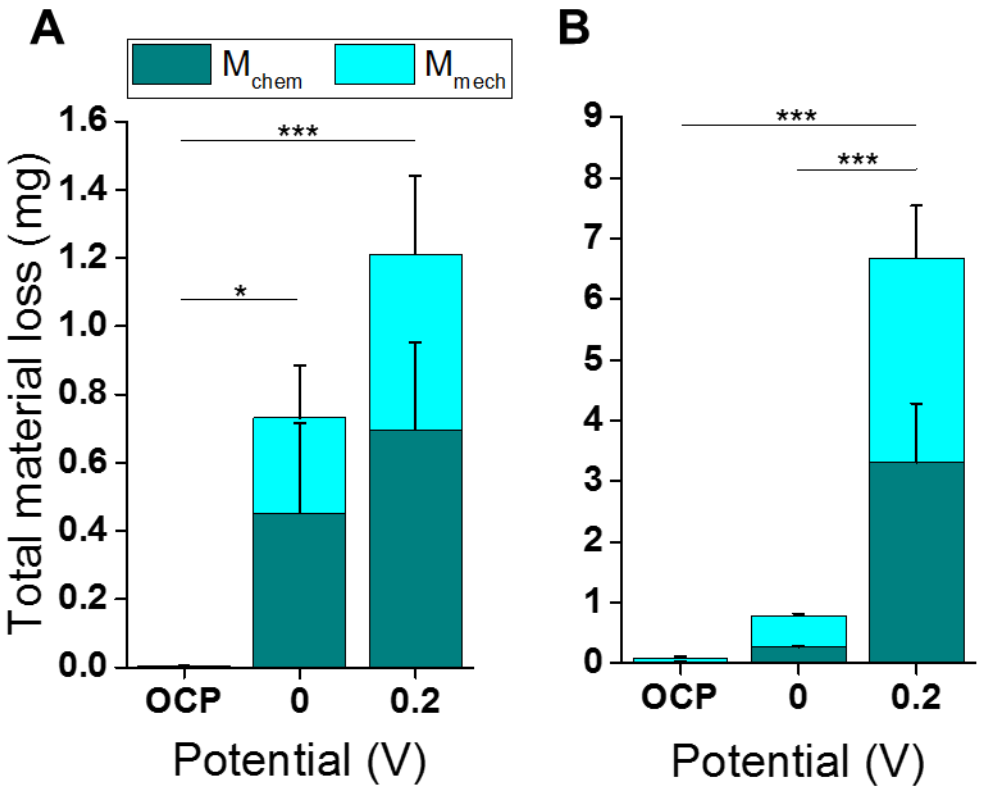

Figure 13. Relative contributions to total wear in terms of mechanical and chemical degradation mechanisms for A) CoCrMo and B) NiTi alloy in three polarisation regimes (OCP, 0V and 0.2V) during 80,000 fretting cycles (n=3). Data shown is mean ± 95% confidence intervals. Total wear significance shown with one-way ANOVA with post-hoc Tukey test, *p<0.05, ***p<0.001.

5.2 The roles of applied potential on fretting mechanisms

The effect of applied over potential on the tribology at an interface has been well documented in sliding contacts. Ponthiaux et al (56) showed the variation of the coefficient of friction, μ, at different applied potentials and hypothesised the coefficient of friction to be linked to lowest zero current potential because 'mechanical depassivation in the contact area is at maximum and leads to the largest total active area'. They also hypothesised that higher coefficient of friction can be associated with passivity. Within a biotribological context, Yan et al (51) demonstrated the roles between applied potential and the coefficient of friction, attributing the complex behaviour to tribo-chemical processes occurring at the metal – protein level.

A similar observation has been observed in this study. For CoCrMo alloy subjected to fretting-corrosion, tangential forces and cumulative dissipated energy were seen to increase with increasing

applied potential. This is in line with other tribocorrosion studies on CoCrMo where the coefficient of friction correlates with applied over-potential (51, 57). In our case we have considered dissipated energy, which considers frictional forces and displacement at the interface, due to the difficulties in determining friction within a fretting contact (58-60). Interestingly, when CoCrMo was subjected to polarisation at 0 and 0.2V, the tangential forces increased with increasing number of cycles (Figure 4B and 4C). It is conceivable that frictional forces increase with increasing number of cycles due to the development of the contact area over the 80,000 cycles. The final nominal contact area is considerably larger than the initial Hertzian contact area calculated with an increased confirmation of the surfaces.

It is evident that the development of the contact area is linked to the corrosion conditions at the contact and will be enhanced by the accelerated corrosion at the interface. In the literature, coefficients of friction ranging from $\mu = 0.1$ to 1 have been quoted for CoCrMo in sliding interfaces (57). Furthermore the formation of and retention of oxides within the contact will influence the evolving tribology; although their roles in a fretting-corrosion contact past third body effects are not well understood and significantly different in nature to tribochemical reactions in sliding contacts.

In the case of NiTi alloy, the effect of applied potential from 0V and 0.2V was not as apparent as for CoCrMo alloy. All NiTi fretting loops showed a gross-slip regime, with some interesting observations between those at OCP and at an applied potential. A slight decrease in $\frac{\delta_s}{\delta_d}$ was observed when compared to CoCrMo-CoCrMo interfaces likely due to the decreased reduced modulus of the NiTi-NiTi contact. As a result, a component of elastic deformation was introduced at the interface, although remained well within the gross-slip criteria as outlined by Fouvry (44). For all three instances of the experiment conducted at OCP the fretting loop shape exhibited a ‘tail-like’ region on the forward stroke. The reasons for this are not fully understood, but are there are some links between the mechanical and electrochemical processes evident. At the wear scar interface there was very localised formation of sulphurous complexes solely at OCP, perhaps going some way towards explaining the unusual fretting-loop shape – as they are so localised, the tangential force peaks over the course of the fretting cycle as it interacts with them. Fretting loops at 0 and 0.2V presented a more conventional appearance with evidence of plastic pile up at the edges of the contact, causing the tangential force to increase rapidly

556 towards the end of the stroke (59). This is supported by Figure 9 which shows evidence of debris build-
557 up at the edges of the contact. Due to the lack of fretting loop analysis for NiTi in physiological media,
558 this phenomenon cannot be entirely explained. The root cause for this is unclear and further work to
559 understand if this relates to a strain related transformation of the NiTi or localised build-up of debris
560 within the contact is needed. No trend in the magnitude of tangential forces at the different polarisation
561 conditions and with increasing number of cycles could be observed, in contrast to CoCrMo. Overtime,
562 the rate of cumulative energy dissipation was seen to decrease suggesting a change in the degradation
563 rate or mechanism at the interface. This may arise from the unique austenitic – martensitic strain-rate
564 dependant transformation characteristics that NiTi alloys possess (61). It is conceivable that cyclic
565 loading and fatigue at the interface will induce cumulative changes in the subsurface micro-structure
566 effecting the evolution of mechanical and corrosive damage over time.

567 **5.3 The role of applied potential on ionic and particulate debris formation.**

568 In both metallic alloy cases, the debris and ion release was altered in terms of both chemistry and
569 morphology with the application of electrochemical over-potential. The elements making up the bulk
570 metal substrate (Co, Cr and Mo) were not detected when undertaking SEM-EDX analysis at OCP, but
571 instead provided signals for O, P and Ca. These were also present on the wear scar surface, indicating
572 that at OCP the removed wear debris consists of the passive layer formed continuously from abrasion
573 and retained in the contact during fretting (62). With the application of over-potential, the elemental
574 composition of the debris was seen to vary when compared to debris retrieved OCP. Cr, O and P rich
575 debris was observed, similar to that retained within the contact. A similar observation was seen of the
576 NiTi, with the application of over-potential influencing the nature and chemistry of the debris produced.
577 At OCP, debris mainly consisting of Ni, Ti, and O was observed. The nature of the debris produced was
578 seen to be altered with the application over potential during fretting-corrosion, with Ti, O, P and Ca
579 rich particulates being observed at 0.2V. Without a doubt, the application of an applied electrochemical
580 potential influences the nature of the debris generated at an interface, intrinsically linked to the changes
581 tribological processes discussed above and the changes in passive film chemistry. It is well established
582 that the application of over-potential influences the nature and quantity of preferentially absorbed

583 species on a surface, the thickness of the oxide film and thermodynamic driving forces for specie
584 migration across the oxide layer. All of these factors will synergistically interact with the tribological
585 processes, influencing the evolving degradation mechanism and nature of the debris produced. Whilst
586 there is not a great deal of literature observing the nature and chemistry of debris derived from fretting-
587 corrosion interfaces, the observations for CoCrMo correlate well with particle analysis retrieved from
588 in-vivo orthopaedic implants. Cr and P rich particles have been observed in peri-implant soft tissues
589 and hypothesised to arise from fretting interfaces which is consistent with this study (63). The nature
590 NiTi debris is still yet to be fully understood.
591 Perhaps one of the most interesting observations made in this study is the variation in ion release
592 stoichiometry with applied over-potential. For CoCrMo-CoCrMo fretting interfaces, the ion release
593 stoichiometry changed from chromium-dominated to cobalt-dominated with the proportion of cobalt
594 ions increasing with polarisation potential. Similarly for NiTi-NiTi interfaces, this went from a near
595 stoichiometric release of Ni and Ti to a Ni dominated solution. This may be explained by the reliance
596 of biomedical alloys to form a passive surface layer to protect against corrosion, the changes in the
597 oxide film characteristics and nature of species absorbed at the interface as a result of polarisation (26).
598 In the particular case of CoCrMo and NiTi, this is typically a chromium-oxide and titanium-oxide rich
599 layer respectively (64, 65). Cyclic abrasion of the surfaces and retention of the debris within the
600 interface is supported by both the wear scar chemistry and that of the wear particles. In both cases a
601 correlation between the elemental composition of the debris and stoichiometry could be observed
602 suggesting. For CoCrMo-CoCrMo contacts, where Cr rich debris was observed (Figure 11C and E),
603 Cobalt dominated ion release was observed. This suggest that the mobility and of Co and Cr at the
604 interfaces differs based on the electrochemical and tribological conditions at the interface. A similar
605 observation was made for NiTi-NiTi interfaces. Ni dominated ion release was observed at 0.2V whereas
606 the debris was Ti, O, P and Ca rich. In both cases, Cr and Ti are thermo-dynamically favourable
607 reactions contributing the reformation of oxide layer once abraded (66). An initial release of Ni and Co
608 will likely occur when the nascent metallic surface is exposed to the electrolyte until an effective oxide
609 layer is formed, enabling the soluble Ni and Co to migrate from the interface. This will depend on the
610 electrode potential and pH at the interface. This further points to the importance of considering the

nature of the test environment and experimental conditions on the debris generation mechanisms at an interface.

The enhanced metal ion release due to tribological processes has been reported mainly for sliding contacts, which significantly differ to fretting-corrosion interfaces. Espallargas *et al.* showed that ion release was dominated by cobalt under sliding-corrosion at OCP and cathodic and anodic polarisation (35). However, the interface in this study was a sliding (6 mm stroke length) CoCrMo-alumina interface as opposed to a fretting CoCrMo-CoCrMo contact. In a hip implant head/cup large sliding interface ion dissolution was shown to be stoichiometric rather than cobalt-dominated(67). Molybdenum in terms of ion release, wear scar chemistry and presence in wear particles also appeared to be relatively unaffected by polarisation. However it has previously been shown that molybdenum dissolution is significantly impacted by presence of proteins which were absent from this study (35, 49).

5.4 Concluding remarks

Metallic biomaterials are commonly and widely used for cardiovascular stents and well as other areas of biomedical engineering. Although there is *in vivo* evidence of wear debris release at the strut interface of braided designs (12, 68), to the authors' knowledge there is no literature detailing the links between fretting-corrosion processes and the nature of the resultant debris. To investigate tribocorrosion mechanisms in biomaterials, studies have used potentiostatic polarisation to exacerbate material degradation during fretting. This study shows that the nature of the wear debris, from particle chemistry and morphology to ion release, is affected by the polarisation potential. In the case of CoCrMo, the wear debris was intrinsically altered during polarisation under fretting despite the maintenance of the tribological and electrochemical characteristics. However NiTi was particularly susceptible to wear-enhanced corrosion as polarisation potential was increased, affecting the tribocorrosion mechanism itself and the wear debris.

Gaining an appreciation of the stent in the physiological environment is imperative to elucidating the material degradation mechanisms occurring in stents *in vivo* and the biological impact of released debris. As proven in hip orthopaedic implants, wear debris and its morphology and composition may have unexpected and devastating consequences for patients (14, 17, 69). In the case of vascular stents,

it has been shown that fretting-corrosion and local release of wear debris to tissues occurs *in vivo* (12, 68). This is hypothesised to be a compounding factor in the most common mechanism of stent failure, in-stent restenosis which is a biologically mediated phenomenon. Studies aiming to understand the biological effects of fretting-corrosion must therefore attempt to replicate the physiological scenario. This study shows that undertaking fretting-corrosion experiments under potentiostatic control as opposed to at the materials open circuit potential both CoCrMo and NiTi alloys affected the degradation mechanisms and released wear debris. It can be appreciated that useful triboelectrochemical techniques may inherently alter the system. Future work in this area will be focussed on the biological impact of wear debris under different polarisation regimes and the compounding factors of presence of serum proteins and inflammatory mediators.

6. Conflicts of interest

The authors have no conflicts of interest to disclose.

7. Funding sources

This work was supported by the Engineering and Physical Sciences Research Council (EP/P009662/1).

8. References

1. BUCCHERI, D., D. PIRAINO, G. ANDOLINA and B. CORTESE. Understanding and managing in-stent restenosis: a review of clinical data, from pathogenesis to treatment. *Journal of Thoracic Disease*, 2016, **8**(10), pp.E1150-E1162.
2. NAGHI, J., E.A. YALVAC, A. POURDJABBAR, L. ANG, J. BAHADORANI, R.R. REEVES, E. MAHMUD and M. PATEL. New developments in the clinical use of drug-coated balloon catheters in peripheral arterial disease. *Med Devices (Auckl)*, 2016, **9**, pp.161-74.
3. LOWE, H.C., S.N. OESTERLE and L.M. KHACHIGIAN. Coronary in-stent restenosis: Current status and future strategies. *Journal of the American College of Cardiology*, 2002, **39**(2), pp.183-193.
4. MITRA, A.K. and D.K. AGRAWAL. In stent restenosis: bane of the stent era. *Journal of Clinical Pathology*, 2006, **59**(3), pp.232-239.
5. DANGAS, G.D., B.E. CLAESSEN, A. CAIXETA, E.A. SANIDAS, G.S. MINTZ and R. MEHRAN. In-stent restenosis in the drug-eluting stent era. *J Am Coll Cardiol*, 2010, **56**(23), pp.1897-907.
6. XU, J., J. YANG, S. SOHRABI, Y. ZHOU and Y. LIU. Finite Element Analysis of the Implantation Process of Overlapping Stents. *Journal of Medical Devices*, 2017, **11**(2), pp.021010-021010-9.
7. KAPNISIS, K.K., D.O. HALWANI, B.C. BROTT, P.G. ANDERSON, J.E. LEMONS and A.S. ANAYIOTOS. Stent overlapping and geometric curvature influence the structural

integrity and surface characteristics of coronary nitinol stents. *Journal of the Mechanical Behavior of Biomedical Materials*, 2013, **20**, pp.227-236.
8. JIN, Z.M., J. ZHENG, W. LI and Z.R. ZHOU. Tribology of medical devices. *Biosurface and Biotribology*, 2016, **2**(4), pp.173-192.
9. HALWANI, D.O., P.G. ANDERSON, B.C. BROTT, A.S. ANAYIOTOS and J.E. LEMONS. The role of vascular calcification in inducing fatigue and fracture of coronary stents. *Journal of Biomedical Materials Research Part B: Applied Biomaterials*, 2012, **100B**(1), pp.292-304.
10. TRÉPANIER, C., X.Y. GONG, T. DITTER, A. PELTON, Y. NEELY and R. GRISHABER. Effect of wear and crevice on the corrosion resistance of overlapped stents. *In: SMST-2006 - Proceedings of the International Conference on Shape Memory and Superelastic Technologies*, 2008, pp.265-276.
11. KAPNISIS, K.K., D.O. HALWANI, B.C. BROTT, P.G. ANDERSON, J.E. LEMONS and A.S. ANAYIOTOS. Stent overlapping and geometric curvature influence the structural integrity and surface characteristics of coronary nitinol stents. *Journal of the Mechanical Behavior of Biomedical Materials*, 2013, **20**(0), pp.227-236.
12. HALWANI, D.O., P.G. ANDERSON, B.C. BROTT, A.S. ANAYIOTOS and J.E. LEMONS. Clinical device-related article surface characterization of explanted endovascular stents: Evidence of in vivo corrosion. *Journal of Biomedical Materials Research Part B: Applied Biomaterials*, 2010, **95B**(1), pp.225-238.
13. RIEPE, G., C. HEINTZ, E. KAISER, N. CHAKFÉ, M. MORLOCK, M. DELLING and H. IMIG. What can we learn from explanted endovascular devices? *European Journal of Vascular and Endovascular Surgery*, 2002, **24**(2), pp.117-122.
14. HALLAB, N.J. and J.J. JACOBS. Biologic effects of implant debris. *Bulletin of the NYU hospital for joint diseases*, 2009, **67**(2), p.182.
15. BINGMANN, D., M. VORPAHL, M. WIEMANN and H. BRAUER. Effects of metal ions on proliferation of aortic smooth muscle cells and myoblastic cells in vitro. *Materialwissenschaft und Werkstofftechnik*, 2001, **32**(12), pp.970-975.
16. SHIH, C.C., S.J. LIN, Y.L. CHEN, Y.Y. SU, S.T. LAI, G.J. WU, C.F. KWOK and K.H. CHUNG. The cytotoxicity of corrosion products of nitinol stent wire on cultured smooth muscle cells. *J Biomed Mater Res*, 2000, **52**(2), pp.395-403.
17. PAPAGEORGIOU, I., C. BROWN, R. SCHINS, S. SINGH, R. NEWSON, S. DAVIS, J. FISHER, E. INGHAM and C.P. CASE. The effect of nano- and micron-sized particles of cobalt-chromium alloy on human fibroblasts in vitro. *Biomaterials*, 2007, **28**(19), pp.2946-58.
18. DRYNDA, S., A. DRYNDA, B. FEUERSTEIN, J. KEKOW, C.H. LOHMANN and J. BERTRAND. The effects of cobalt and chromium ions on transforming growth factor-beta patterns and mineralization in human osteoblast-like MG63 and SaOs-2 cells. *Journal of Biomedical Materials Research Part A*, 2018, **106**(8), pp.2105-2115.
19. NINOMIYA, J.T., S.A. KUZMA, T.J. SCHNETTLER, J.G. KROLIKOWSKI, J.A. STRUVE and D. WEIHRAUCH. Metal ions activate vascular endothelial cells and increase lymphocyte chemotaxis and binding. *J Orthop Res*, 2013, **31**(9), pp.1484-91.
20. SHIH, C.C., C.M. SHIH, Y.L. CHEN, Y.Y. SU, J.S. SHIH, C.F. KWOK and S.J. LIN. Growth inhibition of cultured smooth muscle cells by corrosion products of 316 L stainless steel wire. *J Biomed Mater Res*, 2001, **57**(2), pp.200-7.
21. MCLUCAS, E., Y. ROCHEV, W.M. CARROLL and T.J. SMITH. Analysis of the effects of surface treatments on nickel release from nitinol wires and their impact on candidate gene expression in endothelial cells. *J Mater Sci Mater Med*, 2008, **19**(3), pp.975-80.
22. WINN, B., J.C.D. QUARLES, R.K. MARCUS and M. LABERGE. Nickel ions inhibit α-actin expression and decrease aspect ratio of rat vascular smooth muscle cellsin vitro. *Metallomics*, 2011, **3**(9), pp.934-940.
23. ROYHMAN, D., M. PATEL, M.J. RUNA, M.A. WIMMER, J.J. JACOBS, N.J. HALLAB and M.T. MATHEW. Fretting-corrosion behavior in hip implant modular junctions: The influence of friction energy and pH variation. *Journal of the Mechanical Behavior of Biomedical Materials*, 2016, **62**, pp.570-587.

24. GOLDBERG, J.R. and J.L. GILBERT. The electrochemical and mechanical behavior of passivated and TiN/AlN-coated CoCrMo and Ti6Al4V alloys. *Biomaterials*, 2004, **25**(5), pp.851-864.
25. SWAMINATHAN, V. and J.L. GILBERT. Fretting corrosion of CoCrMo and Ti6Al4V interfaces. *Biomaterials*, 2012, **33**(22), pp.5487-5503.
26. VALERO VIDAL, C. and A. IGUAL MUÑOZ. Electrochemical characterisation of biomedical alloys for surgical implants in simulated body fluids. *Corrosion Science*, 2008, **50**(7), pp.1954-1961.
27. CAO, S., A.I. MUÑOZ and S. MISCHLER. Rationalizing the In Vivo Degradation of Metal-on-Metal Artificial Hip Joints Using Tribocorrosion Concepts. *CORROSION*, 2017, **73**(12), pp.1510-1519.
28. BARRIL, S., S. MISCHLER and D. LANDOLT. Electrochemical effects on the fretting corrosion behaviour of Ti6Al4V in 0.9% sodium chloride solution. *Wear*, 2005, **259**(1), pp.282-291.
29. MISCHLER, S. Triboelectrochemical techniques and interpretation methods in tribocorrosion: A comparative evaluation. *Tribology International*, 2008, **41**(7), pp.573-583.
30. SWAMINATHAN, V. and J.L. GILBERT. Potential and frequency effects on fretting corrosion of Ti6Al4V and CoCrMo surfaces. *Journal of Biomedical Materials Research Part A*, 2013, **101A**(9), pp.2602-2612.
31. DIMAH, M.K., F.D. ALBEZA, V.A. BORRAS and A.I. MUNOZ. Study of the biotribocorrosion behaviour of titanium biomedical alloys in simulated body fluids by electrochemical techniques. *Wear*, 2012, **294**, pp.409-418.
32. HIROMOTO, S. and S. MISCHLER. The influence of proteins on the fretting–corrosion behaviour of a Ti6Al4V alloy. *Wear*, 2006, **261**(9), pp.1002-1011.
33. ALONSO GIL, R. and A. IGUAL MUÑOZ. Influence of the sliding velocity and the applied potential on the corrosion and wear behavior of HC CoCrMo biomedical alloy in simulated body fluids. *Journal of the Mechanical Behavior of Biomedical Materials*, 2011, **4**(8), pp.2090-2102.
34. MISCHLER, S. and P. PONTHIAUX. A round robin on combined electrochemical and friction tests on alumina/stainless steel contacts in sulphuric acid. *Wear*, 2001, **248**(1), pp.211-225.
35. ESPALLARGAS, N., C. TORRES and A.I. MUÑOZ. A metal ion release study of CoCrMo exposed to corrosion and tribocorrosion conditions in simulated body fluids. *Wear*, 2015, **332-333**, pp.669-678.
36. AZZI, M. and J.A. SZPUNAR. Tribo-electrochemical technique for studying tribocorrosion behavior of biomaterials. *Biomolecular Engineering*, 2007, **24**(5), pp.443-446.
37. HESKETH, J., X. HU, Y. YAN, D. DOWSON and A. NEVILLE. Biotribocorrosion: Some electrochemical observations from an instrumented hip joint simulator. *Tribology International*, 2013, **59**, pp.332-338.
38. BILLI, F., P. BENYA, E. EBRAMZADEH, P. CAMPBELL, F. CHAN and H.A. MCKELLOP. Metal wear particles: What we know, what we do not know, and why. *SAS Journal*, 2009, **3**(4), pp.133-142.
39. CHAKFÉ, N. and F. HEIM. Commentary on 'electrical potentials between stent-grafts made from different metals induce negligible corrosion'. *European Journal of Vascular and Endovascular Surgery*, 2013, **46**(4), pp.438-439.
40. BRYANT, M., M. WARD, R. FARRAR, R. FREEMAN, K. BRUMMITT, J. NOLAN and A. NEVILLE. Failure analysis of cemented metal-on-metal total hip replacements from a single centre cohort. *Wear*, 2013, **301**, pp.226-233.
41. RICHES, K., T. ANGELINI, G. MUDHAR, J. KAYE, E. CLARK, M. BAILEY, S. SOHRABI, S. KOROSSIS, P. WALKER, D.J. SCOTT and K. PORTER. Exploring smooth muscle phenotype and function in a bioreactor model of abdominal aortic aneurysm. *Journal of Translational Medicine*, 2013, **11**(1), p.208.

42. RICHES, K., E. CLARK, R.J. HELLIWELL, T.G. ANGELINI, K.E. HEMMINGS, M.A. BAILEY, K.I. BRIDGE, D.J.A. SCOTT and K.E. PORTER. Progressive Development of Aberrant Smooth Muscle Cell Phenotype in Abdominal Aortic Aneurysm Disease. *Journal of Vascular Research*, 2018, **55**(1), pp.35-46.
43. OLADOKUN, A., M. PETTERSSON, M. BRYANT, H. ENGQVIST, C. PERSSON, R. HALL and A. NEVILLE. Fretting of CoCrMo and Ti6Al4V alloys in modular prostheses. *Tribology-Materials, Surfaces & Interfaces*, 2015, **9**(4), pp.165-173.
44. FOUVRY, S., P. KAPSA, H. ZAHOUANI and L. VINCENT. Wear analysis in fretting of hard coatings through a dissipated energy concept. *Wear*, 1997, **203-204**, pp.393-403.
45. BRYANT, M. and A. NEVILLE. Fretting corrosion of CoCr alloy: Effect of load and displacement on the degradation mechanisms. *Proceedings of the Institution of Mechanical Engineers, Part H: Journal of Engineering in Medicine*, 2016, **231**(2), pp.114-126.
46. NEVILLE, A., J. HESKETH, A.R. BEADLING, M.G. BRYANT and D. DOWSON. Incorporating corrosion measurement in hip wear simulators: An added complication or a necessity? *Proceedings of the Institution of Mechanical Engineers, Part H: Journal of Engineering in Medicine*, 2016, **230**(5), pp.406-420.
47. SILVERMAN, D.C. Tutorial on Cyclic Potentiodynamic Polarization Technique. *In: CORROSION 98*, 1998/1/1/, San Diego, California. NACE International, 1998, p.21.
48. STERN, M. and A.L. GEARY. Electrochemical Polarization: I . A Theoretical Analysis of the Shape of Polarization Curves. *Journal of The Electrochemical Society*, 1957, **104**(1), pp.56-63.
49. SIMOES, T.A., M.G. BRYANT, A.P. BROWN, S.J. MILNE, M. RYAN, A. NEVILLE and R. BRYDSON. Evidence for the dissolution of molybdenum during tribocorrosion of CoCrMo hip implants in the presence of serum protein. *Acta Biomaterialia*, 2016, **45**, pp.410-418.
50. FOUVRY, S., P. KAPSA and L. VINCENT. Description of fretting damage by contact mechanics. *ZAMM - Journal of Applied Mathematics and Mechanics / Zeitschrift für Angewandte Mathematik und Mechanik*, 2000, **80**(S1), pp.41-44.
51. YAN, Y., A. NEVILLE and D. DOWSON. Tribo-corrosion properties of cobalt-based medical implant alloys in simulated biological environments. *Wear*, 2007, **263**(7), pp.1105-1111.
52. WATSON, S.W., F.J. FRIEDERSDORF, B.W. MADSEN and S.D. CRAMER. Methods of measuring wear-corrosion synergism. *Wear*, 1995, **181-183**, pp.476-484.
53. LUKINA, E., M. KOLLEROV, J. MESWANIA, A. KHON, P. PANIN and G.W. BLUNN. Fretting corrosion behavior of nitinol spinal rods in conjunction with titanium pedicle screws. *Materials Science and Engineering: C*, 2017, **72**, pp.601-610.
54. KOSEC, T., P. MOČNIK and A. LEGAT. The tribocorrosion behaviour of NiTi alloy. *Applied Surface Science*, 2014, **288**, pp.727-735.
55. C, T., G. XY, D. T, P. A, N. Y and G. R. Effect of wear and crevice on the corrosion resistance of overlapped stents. SMST-2006. *In: International Conference on Shape Memory and Superelastic Technologies*, Menlo Park, CA: SMST Society. 2008, pp.265–275.
56. PONTHIAUX, P., F. WENGER, D. DREES and J.P. CELIS. Electrochemical techniques for studying tribocorrosion processes. *Wear*, 2004, **256**(5), pp.459-468.
57. IGUAL MUÑOZ, A. and S. MISCHLER. Effect of the environment on wear ranking and corrosion of biomedical CoCrMo alloys. *Journal of Materials Science: Materials in Medicine*, 2011, **22**(3), pp.437-450.
58. KIM, K. and J. GERINGER. Analysis of energy dissipation in fretting corrosion experiments with materials used as hip prosthesis. *Wear*, 2012, **296**(1), pp.497-503.
59. PEARSON, S.R., P.H. SHIPWAY, J.O. ABERE and R.A.A. HEWITT. The effect of temperature on wear and friction of a high strength steel in fretting. *Wear*, 2013, **303**(1), pp.622-631.
60. WARMUTH, A.R., P.H. SHIPWAY and W. SUN. Fretting wear mapping: the influence of contact geometry and frequency on debris formation and ejection for a steel-on-

steel pair. *Proceedings of the Royal Society A: Mathematical, Physical and Engineering Science*, 2015, **471**(2178).
61. NEMAT-NASSER, S., J.Y. CHOI, W.-G. GUO, J.B. ISAACS, M.J.J.O.E.M. TAYA and TECHNOLOGY. High strain-rate, small strain response of a NiTi shape-memory alloy. 2005, **127**(1), pp.83-89.
62. FENG, I.M. and B.G. RIGHTMIRE. An Experimental Study of Fretting. *Proceedings of the Institution of Mechanical Engineers*, 1956, **170**(1), pp.1055-1064.
63. DI LAURA, A., P.D. QUINN, V.C. PANAGIOTOPOULOU, H.S. HOTHI, J. HENCKEL, J.J. POWELL, F. BERISHA, F. AMARY, J.F.W. MOSSELMANS, J.A. SKINNER and A.J. HART. The Chemical Form of Metal Species Released from Corroded Taper Junctions of Hip Implants: Synchrotron Analysis of Patient Tissue. *Scientific Reports*, 2017, **7**(1), p.10952.
64. MUÑOZ, A.I. and S. MISCHLER. Interactive Effects of Albumin and Phosphate Ions on the Corrosion of CoCrMo Implant Alloy. *Journal of The Electrochemical Society*, 2007, **154**(10), pp.C562-C570.
65. MILOŠEV, I. and H.H. STREHBLOW. The composition of the surface passive film formed on CoCrMo alloy in simulated physiological solution. *Electrochimica Acta*, 2003, **48**(19), pp.2767-2774.
66. POURBAIX, M. *Atlas of electrochemical equilibria in aqueous solutions*. National Association of Corrosion Engineers, 1974.
67. HESKETH, J., Q. MENG, D. DOWSON and A. NEVILLE. Biotribocorrosion of metal-on-metal hip replacements: How surface degradation can influence metal ion formation. *Tribology International*, 2013, **65**, pp.128-137.
68. HALWANI, D.O., P.G. ANDERSON, J.E. LEMONS, W.D. JORDAN, A.S. ANAYIOTOS and B.C. BROTT. In-vivo corrosion and local release of metallic ions from vascular stents into surrounding tissue. *J Invasive Cardiol*, 2010, **22**(11), pp.528-35.
69. LANGTON, D.J., S.S. JAMESON, T.J. JOYCE, N.J. HALLAB, S. NATU and A.V.F. NARGOL. Early failure of metal-on-metal bearings in hip resurfacing and large-diameter total hip replacement A CONSEQUENCE OF EXCESS WEAR. *Journal of Bone and Joint Surgery-British Volume*, 2010, **92B**(1), pp.38-46.